الجامعة الأردنيـــــة
كلية الدراسات العليا

التاريـــخ: / /

نموذج رقم (١٦)
اقرار والتزام بالمعايير الأخلاقية والأمانة العلمية وقوانين الجامعة الأردنية وأنظمتها وتعليماتها لطلبة الدكتوراه

أنا الطالب: تركي سليمان عبد الرحمن العقرباوي الرقم الجامعي: (٩٠٥٠٤٤٩)
تخصص: الفيزياء الكليـــــة: العلوم

عنوان الاطروحة: I-125 Brachytherapy Source: Characterization of dose Parameters and Medical Applications

اعلن بأنني قد التزمت بقوانين الجامعة الأردنية وأنظمتها وتعليماتها وقراراتها السارية المفعول المتعلقة باعداد اطروحات الدكتوراه عندما قمت شخصيا" باعداد اطروحتي وذلك بما ينسجم مع الأمانة العلمية وكافة المعايير الأخلاقية المتعارف عليها في كتابة الأطروحات العلمية. كما أنني أعلن بأن اطروحتي هذه غير منقولة أو مستلة من أطاريح أو كتب أو أبحاث أو أي منشورات علمية تم نشرها أو تخزينها في أي وسيلة اعلامية، وتأسيسا" على ما تقدم فانني أتحمل المسؤولية بأنواعها كافة فيما لو تبين غير ذلك بما فيه حق مجلس العمداء في الجامعة الأردنية بالغاء قرار منحي الدرجة العلمية التي حصلت عليها وسحب شهادة التخرج مني بعد صدورها دون أن يكون لي أي حق في التظلم أو الاعتراض أو الطعن بأي صورة كانت في القرار الصادر عن مجلس العمداء بهذا الصدد.

توقيع الطالب:.............................. التاريخ: ٨ /١١ / ٢٠١١

The University of Jordan

Authorization Form

I, Tahani Sulaiman Al-Aqrabawi, authorize the University of Jordan to supply copies of my Dissertation to libraries or establishments or individuals on request, according to the University of Jordan regulations.

Signature: Tahani Aqrabawi

Date: 11/8/2011

I-125 BRACHYTHERAPY SOURCE: CHARACTERIZATION OF DOSE PARAMETERS AND MEDICAL APPLICATIONS

By
Tahani Sulaiman Al-Aqrabawi

Supervisor
Dr. Jamal Sharaf

Co-Supervisor
Dr. Saed Dababneh

This Dissertation was Submitted in Partial Fulfillment of the Requirements for the Doctor of Philosophy Degree in Physics

Faculty of Graduate Studies
The University of Jordan

August, 2011

COMMITTEE DECISION

This Dissertation (I-125 Brachytherapy Source: Characterization of Dose Parameters and Medical Applications) was Successfully Defended and Approved on 12/5/2011.

Examination Committee	**Signature**
Dr. Jamal Sharaf (Supervisor) Associate Professor of Medical Physics	…………………………
Dr. Saed Dababneh (Co-Supervisor) Associate Professor of Nuclear Physics	…………………………
Dr. Dia Eddin Arafah (Member) Professor of Solid State Physics	…………………………
Dr. Adnan Mohammad Othman Ismail (Member) Associate Professor of Solid State Physics	…………………………
Dr. Issa Al-Shakhrah (Member) Professor of Medical Physics	…………………………
Dr. Rami Ali (Member) Associate Professor of Experimental Atomic and Molecular Physics	…………………………

DEDICATION

I would like to dedicate this doctoral dissertation to my mother who has been praying for my success in education and in my life. There is no doubt in my mind that without her continued support, I could not have completed this work. It is also dedicated to my father and all my family members, who assisted and encouraged me in various ways. It is also dedicated to everyone who wished me luck.

“Tough times do not last but tough people do”

ACKNOWLEDGEMENT

It is a pleasure to thank the many people who made this thesis possible. I am heartily thankful to my supervisor, Dr.Jamal Sharaf , and to my co-supervisor Dr. Saed Dababneh for encouragement, guidance and support from the initial to the final phases, which enabled me to develop an understanding of the subject.

It is difficult to overstate my gratitude to Dr. Saed Dababneh with his enthusiasm, inspiration, and great efforts to explain things clearly and simply,

Also I offer my regards and blessings to Dr. Shada Ramahi who guided me by very important comments, during the completion of the project. She keeps saying that “there’s always light at the end of the tunnel”.

I am heartily thankful for the decision committee members. For their valuable comments and notes which enabled me to develop and complete this study.

Lastly, and most importantly, I wish to thank my parents. They bore me, raised me, supported me, taught me, and loved me. To them I dedicate this thesis.

Tahani Aqrabawi

LIST OF CONTENTS

LIST OF TABLES

LIST OF FIGURES

I-125 BRACHYTHERAPY SOURCE:

CHARACTERIZATION OF DOSE PARAMETERS AND MEDICAL APPLICATIONS

By

Tahani Sulaiman Al-Aqrabawi

Supervisor

Dr. Jamal Sharaf

Co-Supervisor

Dr. Saed Dababneh

ABSTRACT

Monte Carlo simulation, based on GEANT4 toolkit, has been investigated as an alternative methodology for accurate, assumption free, dose calculation from I-125 brachytherapy sources. This has been achieved by characterization of the source dose parameters. A voxelized water phantom, along with the detailed geometry structure of the source and its encapsulation have been carefully modeled and validated through special codes developed in this work. Comprehensive physics processes have been also implemented. Tracking of secondary particles generated in the simulation was thorough in order to enhance the resolution and accuracy of the location of the registered energy deposition. The dose parameters, namely the radial dose function and the anisotropy function have been successfully determined and compared against published data. As a result, this work has been successful in benchmarking GEANT4 as a toolkit for low energy applications like in medical physics. In addition, comprehensive isodose contours, in different planes and directions, have been constructed. This work constitutes a step for future advances in brachytherapy cancer treatment planning using GEANT4 Monte Carlo simulations.

CHAPTER ONE

INTRODUCTION

1.1 Motivation

The medical use of the iodine radioisotope I-125 in brachytherapy cancer treatment started in the 1980s. The isotope is made into pellets, called seeds and each seed is few millimeters in length. Since brachytherapy is a short distance cancer treatment, dose is prescribed from 5 mm to 20 mm, and in some treatments to no more than 10 mm away from the seed. The implemented dose calculation algorithms suffer from drawbacks and assumptions.

One such assumption was treating the seed as a point source, which is of course invalid due to the closeness of the dose calculation point to the source. In addition, the actual non-uniformity of the distribution of I-125 inside the seed was ignored. The inaccuracy of such point source approximation affects both the absolute dose value as well as the isodose line distribution around the seed. Therefore, unrealistic circular isodose lines concentrically surround the point source, while for the actual extended source, the isodose lines should be elongated and follow the length of the seed. Therefore, anisotropic dose distribution is expected which reflects the distribution of radioactivity within the seed.

In the plaque brachytherapy treatment, seven to 24 seeds are temporarily implanted in the eye. The corresponding inaccuracy due to the point source approximation will therefore add up, making dose calculations even worse. An early study (Astrahan, et al., 1989) showed that for patients treated with I-125 for eye cancer, loss of vision was a real problem due to the radiation retinopathy. The high incidence of late complications suggests that careful treatment optimization may lead to improved outcomes.

A later work by Ray, et al. (1998) revised the Task Group number 43 dosimetry recommendations for I-125 seeds. They studied the effects of the recommendations on the absorbed dose for some patients who have undergone eye plaque therapy. For three representative plaques chosen, the seeds were approximated by isotropic point and line sources, and absorbed doses were calculated at all points on the central axis of the plaque. They found that TG-43 recommendations would result in 6–13% lower absorbed doses unless the dose prescription is modified. Clinicians should be aware of the dosimetric implications of these recommendations if the seeds are approximated by isotropic point sources.

Therefore, accurate dose measurements are essential in all brachytherapy treatments, otherwise results will not be as planned. In such cases, and instead of the intended cancer treatment, other problems could be encountered.

The dosimetry formalism, and changes in calibration standards recommended by TG-43 to be used in clinical practice are related to:

1. Pre-treatment scope through planning, especially concerning temporary implantation time, choosing both the suitable radioisotope and seed model to cope with the desired energy, in addition to predicting clinical outcomes.
2. Post-treatment through clinical outcome evaluation, and accurate calculation of the dose delivered to tumor and to normal tissue.

The above considerations shed light on the significance of this work. We aim at evaluating the dosimetric characteristics of one commercially available I-125 seed through accurate dose calculation. Specifically, we look to comprehensively study the dose distribution around the seed.

1.2 Previous Studies

In an early stage, Burns and Raeside (1983) have used Monte Carlo methods in order to estimate the dose up to 10 cm from an I-125 point source in water. Simulated results were compared to published specific absorbed fraction using the moments method (Berger, 1968). In their simulation, photons were tracked until they escaped from the water phantom, which was a sphere 20 cm in radius. By contrast, we use the comprehensive Monte Carlo GEANT4 toolkit in order to accurately account for the seed geometry and composition. We are able to obtain better statistics due to the larger number of generated primary events. In addition, we are interested in the much smaller distance range of 0.5-1.0 cm around the source. Therefore, we shall use a high resolution grid which implies dividing the phantom into smaller voxels.

In a very recent study (Taylor and Rogers, 2008), EGSnrc Monte Carlo code has been used. A modified fifth order polynomial fitting of the radial dose function g(r), for both I-125 and Pd-103 brachytherapy seeds, was presented as:

$$g(r) = (a_0 r^{-2} + a_1 r^{-1} + a_2 + a_3 r + a_4 r^2 + a_5 r^3) e^{-a_6 r}.$$

The study covers ranges as large as 0.05 to 10.00 cm for I-125 seeds, and 0.1-10.0 cm for Pd-103 seeds. Results have been compared to the TG-43, and to the published results of (Meigooni, et al., 2002). Their new function provides a much better fitting quality than the fifth order polynomial recommended by TG-43. Excellent fits to the radial dose function of different brachytherapy seeds have been achieved, with average discrepancies between the Monte Carlo data and the fitting function of less than 0.4%.

Another study (Meigooni, et al., 2002) used a different modified polynomial written as:

$$g(r) = (a_0 + a_1 r + a_2 r^2 + a_3 r^3 + a_4 r^4 + a_5 r^5) e^{-a_6 r}.$$

The average

discrepancies between fitted and calculated data were found to be less than 0.5% over the full range, with maximum discrepancy of 2%. The fitting function was also capable of accounting for the sharp increase in g(r) (upturn) observed for some sources at $r < 0.1$ cm. This upturn has previously been attributed to the breakdown of the approximation of the source as a line. However, they demonstrated that another contributing factor is the 4.5 keV characteristic x-rays emitted from the Ti seed casing. Fitting coefficients of the new function were tabulated. Extrapolation characteristics of the function were also investigated. The new function was a candidate for fitting the radial dose function of all Pd-103 and I-125 brachytherapy seeds, and increases the accuracy of dose distribution calculated around brachytherapy seeds using the TG-43 protocol over a wider range of data. More accurate values of g(r), for $r < 0.5$ cm, may be particularly important in the treatment of ocular melanoma. Our study performs the same procedure as (Taylor and Rogers, 2008) to find the fitting parameters g(r) for I-125 seed. However, we concentrate on the near distance range (0.5 - 1cm), and we use different I-125 seed. In addition, we seek to find the fitting parameters of $F(r,\theta)$.

An investigation by Kubo (1983) reported the results of exposure measurements for two types of clinical I-125 seeds: a model 6702 no-marker seed, and a model 6711 silver wire seed. Measurements were made locally with a parallel-plate mammography chamber, traceable to the National Bureau of Standards (NBS) calibration. The same seeds were also measured at NBS using a reentrant chamber that was developed and calibrated there. The mammography chamber measurements showed an approximately 5% higher exposure rate for the no-marker seed than the reentrant chamber measurements. On the silver wire seed, good agreement was obtained between the two techniques. It was found that exposure rate variations in the plane perpendicular to the long axis of the seed (or seed axis) were substantial, due in part to the nonsymmetrical

distribution of radioactive material in the seed. In his study, Kubo investigated the effect of the Titanium ends on the photon emission of I-125, and found that Ti contributes characteristic X-rays. His work was conducted only in air surroundings.

In his other study, Kubo (1984) noticed that I-125 yields three intrinsic photons, namely the Te K_α x-ray at 27.4 keV, K_β x-ray at 31.0 keV, and 35.5 keV gamma-rays. In addition, silver wire type seed is known to have both Ag K_α 22.1 keV and K_β 25.2 keV x-rays that result from the interaction between silver atoms and the intrinsic photons. Since radioactive iodine-125 is completely sealed with 0.5 mm thick Titanium capsule, fluorescent x-rays from Titanium atoms are also expected. The study aimed at assessing the exposure contribution from the Ti K x-rays through two steps: The first is the experimental determination of the abundance of Te K_α x-ray photons in order to predict their exposure contribution. The second step is to interpose an attenuator between the source and the detector, removing Ti K x-rays. Combining the two steps one can estimate the exposure due to Ti K x-rays. The study reports the abundance of Ti K x-rays at 4.5 keV, and the contribution to exposure from these photons as amounting to approximately 19% of the total exposure at 1 cm source to detector distance (SDD).

Another study by Sahoo and Selvam (2009) of Titanium-encapsulated I-125 brachytherapy sources was motivated by the fact that the photoelectric interaction of I-125 photons with titanium encapsulation generates about 5 keV Ti K X-rays. According to the National Institute of Standards and Technology (NIST) air-kerma strength S_k standard, these x-rays should be excluded from S_k. Sahoo and Selvam (2009) used the EGSnrc Monte Carlo code to calculate S_k including the contribution of the 5 keV x-rays, dose rate constant, and radial dose function, for five different I-125 source models. Depending upon the source model, the contribution of 5 keV Ti X-rays to S_k varies between 17.1% and 18.7%. Including X-rays as part of S_k would result in

underestimation of the dose rate constant by up to 19%. The radial dose functions of the investigated sources are comparable to published studies that are based on an updated photon cross-section dataset.

In a study presented by Solberg et al. (2002), Monte Carlo MCNP calculations and Thermoluminescent Dosimeter (TLD) measurements have been performed for the purpose of characterizing dosimetric properties of new commercially available brachytherapy sources. All sources tested consisted of a solid core, upon which a thin layer of I-125 has been adsorbed. The PharmaSeed BT-125 source manufactured by Syncor is available in silver or palladium core configurations while the ADVANTAGE source from IsoAid has only silver. The source was encased within titanium housing. Dosimetric properties, including the dose rate constant, radial dose function, and anisotropy characteristics were determined according to the TG-43 protocol. Additionally, the geometry function was calculated using Monte Carlo and compared to both the point and line source approximations. The 1999 NIST standard was followed in determining air kerma strength. Dose rate constants were calculated. TLD measurements were in excellent agreement with Monte Carlo calculations. Radial dose function $g(r)$ was calculated to a distance of 10 cm, and anisotropy function, $F(r,\theta)$, was calculated for radii from 0.5 to 7.0 cm. All dosimetric parameters were found to be in close agreement with previously published data for similar source configurations. The study concluded that MCNP Monte Carlo code appears to be suited to low energy dosimetry applications. To compare with, this work aims at the characterization of the radial dose function $g(r)$, and anisotropy function $F(r,\theta)$, according to the TG-43 protocol. We use a different MC toolkit, namely GEANT4. Our seed design is also different, it is Bebig model I25.S06.

In a study by Sowards and Meigooni (2002), the authors used PTRAN Version 6.3 Monte Carlo to simulate dosimetric parameters of the Bests Model 2301 brachytherapy source. The results of this evaluation indicate the value of dose rate constant of 1.01±3% $cGyh^{-1}U^{-1}$ in liquid water, which is in good agreement with 1.02±8% $cGyh^{-1}U^{-1}$ reported by Nath and Yue (2002). The anisotropy constant was found to be 0.98 in liquid water.

Sowards (2007) studied both I-125 and Pd-103 brachytherapy sources due to their usage in cancer treatment. Various dosimetric parameters have been determined. Theoretical calculations of dosimetric characteristics, dose rate constant, radial dose function, and anisotropy function for the source followed TG-43 recommendations. Calculations were performed in liquid water using the PTRAN Monte Carlo code ver. 7.44. The radial dose function was calculated at distances up to 10.0 cm, and the anisotropy function, at distances ranging from 0.5 to 7.0 cm. The anisotropy factors and anisotropy constant were derived from the anisotropy function. The results in water indicate that the dose rate constant is 0.709 ± 0.014 $cGyh^{-1}U^{-1}$ and that the anisotropy constant is 0.880±0.040. The dosimetric characteristics of this new source compare favorably with those of other commercially available Pd-103 sources.

In an investigation by Burns and Raesid (1989), Monte Carlo MCNP toolkit was applied on seeds immersed in a water phantom, in order to study the perturbation of single I-125 seed dose distribution created by the presence of one or three neighboring seeds. Perturbation factors were determined within the geometric shadow of neighboring seeds, for two seeds design, four seeds spacing, and several choices of dose points. The results were compared to dose estimates obtained by superposition of single seed data for one and two plane implants. Some significant differences were found.

Rivard et al. (2004) and Nath et al. (1995) reported on data for I-125 and Pd -103 source models. They evaluated as many as 12 sets of independently published data per source model, some were Monte Carlo based and others were experimentally acquired. For each source model, a single consensus dataset was derived from multiple published datasets. This consensus dataset was obtained from the peer-reviewed literature which was examined to identify candidate dose distributions for each source model derived either from experimental measurements or Monte Carlo simulations. It was found that not all authors agreed on certain fitting parameters, as well as there were incomplete data for certain seed types. "Inadequate spatial resolution may result in inaccurate interpolation by brachytherapy treatment planning systems, unnecessarily giving rise to dose-delivery errors. Therefore, it is necessary to recommend minimum spatial resolutions and ranges for which these parameters should be specified".

While low energy photon emitting brachytherapy sources have been used to treat different types of cancers, several studies have shown that clinical outcomes of brachytherapy cancer treatment correlate with dose coverage parameters (Rivard, et al., 2004).

Our work establishes a complete set of fitting parameters for I-125 source seed used in plaque brachytherapy, especially for the near-distance region.

1.3 Objectives of This Work

We pursue the effort to accurately characterize I-125 for brachytherapy treatment per the recommendation of TG-43. We aim at benchmarking GEANT4, which is mainly a high energy physics code, for use in low-energy physics; our I-125 source being in the low energy range. Next, the dosimetric parameters of I-125 will be calculated from the outcome of our seed Bebig model I25.S06 interaction in water, as per the GEANT4 toolkit. The dosimetric quantities of interest are two:

a) $F(r,\theta)$: The anisotropy function accounts for the variations on the isodose lines around the seed brought by the distribution of radioactivity within the seed, and the various materials that are used to coat the source and seal the seed.

b) $g(r)$: The radial dose function. It describes the dose fall-off on the transverse plane due to photon attenuation in the medium.

The above dosimetric quantities are measured for the actual design of the seed as obtained from the manufacturer.

CHAPTER TWO
THEORETICAL BACKGROUND

2.1 Brachytherapy

Brachytherapy, sometimes referred to as curie therapy or endocurie therapy, is a term used to describe the short distance treatment of cancer with radiation from small encapsulated radionuclide sources. This type of treatment is given by placing radioactive sources directly into or near the volume to be treated. This enables clinicians to deliver a high dose with minimal impact on surrounding healthy tissues (Suntharalingam, et al., 2006).

The dose is delivered continuously; either over a short period of time (temporary implants) as in the treatment of the eye cancer, or over the lifetime of the source to a complete decay (permanent implants) as in the treatment of prostate cancer.

Figure 2.1.1 illustrates permanent prostate implantation with radioactive I-125 seeds. Needles with the seeds in them are pushed through the skin, and then the seeds are deposited inside the prostate.

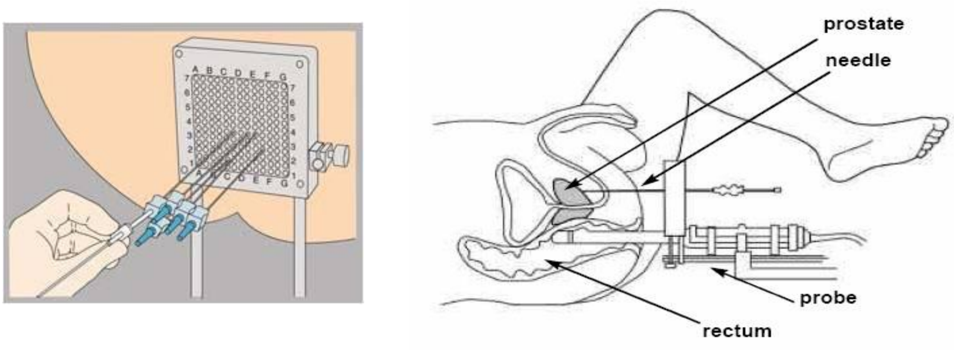


Fig 2.1.1. Method of prostate treatment with radioactive seed implantation.

Images taken from (http://www.prostatebrachytherapyinfo.net/PAT21.html).

In the treatment of prostate cancer, between 60 - 120 seeds are passed through the needles, either individually, or as strands of several seeds linked together. When the seeds are in the correct place, the needles are removed leaving the seeds behind. The seeds stay in the prostate, slowly giving out radiation until they are no longer radioactive (Frank, et al., 2007).

On the other hand, the treatment of eye tumors is an example of temporary implantation. Seeds are loaded into an applicator, called plaque, which is made of gold and plastic. Figure 2.1.2 illustrates an eye plaque applicator.

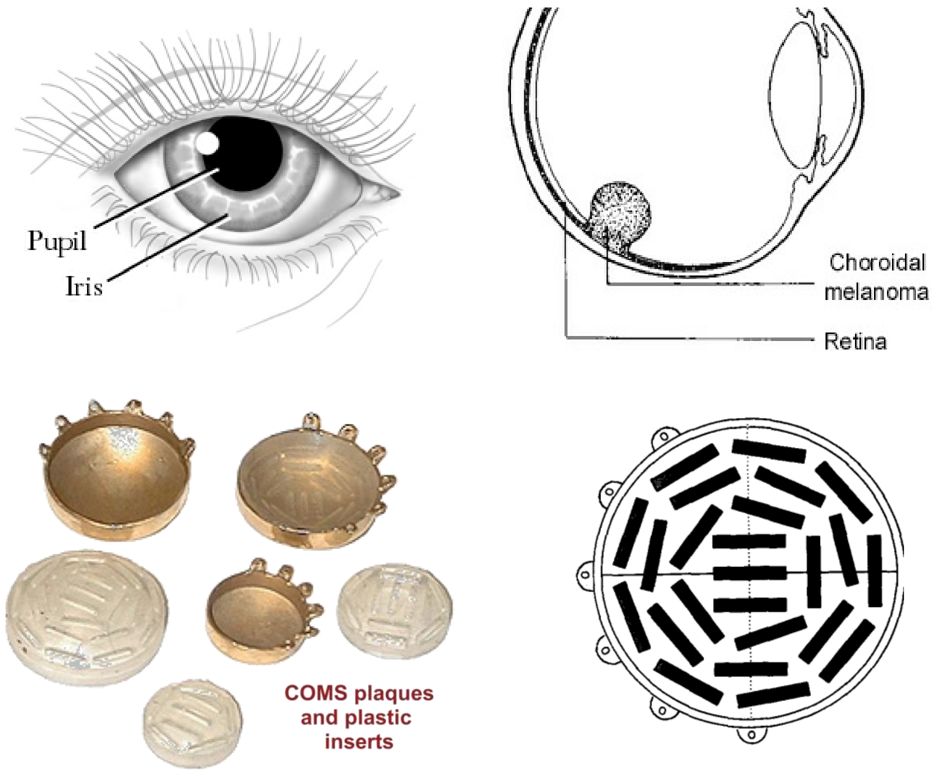


Fig 2.1.2. The eye plaque for treatment of eye tumors.

Images taken from (http://www-naweb.iaea.org/nahu/dmrp/pdf_files/slides/Ch_13_MacForm.pdf).

Various radioisotopes are used in brachytherapy. Table 2.1 lists those most common radioisotopes, including the famous three low energy brachytherapy sources, namely Cs-131, Pd-103 and I-125. The weighted average energy values for these sources are less than 50 keV.

Table 2.1.Some radioisotopes used in brachytherapy (Shleien, et al., 1998) & (http://www.nndc.bnl.gov/).

Radionuclide	**Half-life**	**Weighted Average Energy (keV)**	**Emitted Radiation**	**Emitted Energy (keV)**		
I-125	60 d	28	Electron	3.19 3.68 22.7	34.5 35.3	35.5 30.6
			Gamma	35.5	*	*
			Beta +	150	*	*
			X-ray	3.77 27.2	30.9 27.5	31 31.7
Cs-131	10 d	30	Electron	3.43	24.6	*
			X-ray	4.11 29.5	29.8 33.6	34.4
			Beta +	352	*	*
Pd-103	17 d	21	Gamma	62.4 497	295 444	318 357
			X-ray	2.7	20.1	22.7
			Beta +	6.27	186	248 503
			Electron	2.39 241 272 354 357	16.5 61.8 292 334 474 294	52.7 59 314 317 494 496
Co-60	5.271 y	1250	Gamma	347 2506	826 2159	1173 1333
			X-ray	0.85	7.46 1	7.478 8.265
			Beta -	1491	318	*
			Electron	0.84 825 1165 2150 2158	6.54 818 1172 1332 2497 1333	339 346 1173 1324 2505 2506
Cs-137	30.17 y	662	Gamma	284	*	*
			Beta	514	892	1176

2.2 Brachytherapy Treatments

2.2.a Brachytherapy Treatments with regard to the Type of Implants

- Intracavitary: Sources are placed into body cavities close to the tumor volume. Figure 2.2.a.1 illustrates treatment of nasopharyngeal cancer. Gynecological treatments also fall under this type.

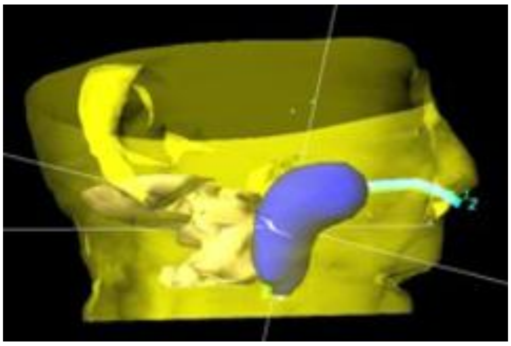


Fig 2.2.a.1. Intracavitary implant for a nasopharyngeal cancer.

Image taken from (http://radonc.ucla.edu/body.cfm).

- Interstitial: Sources are implanted surgically within the tumor volume, as shown in Figure 2.2.a.2. Tongue, floor of mouth, tonsil, cheek, and prostate are examples of interstitial implants.

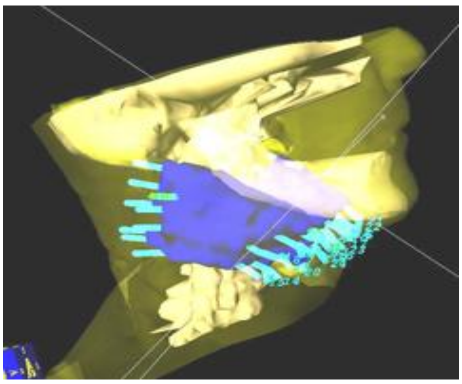


Fig 2.2.a.2 Interstitial implant for base of tongue cancer and right neck lymph node.

Image taken from (http://radonc.ucla.edu/body.cfm).

- Surface plaque: Sources are loaded into a plaque which is brought into contact with a skin surface lesion. Examples are the treatment of eye tumors and skin (Figure 2.2.a.3).

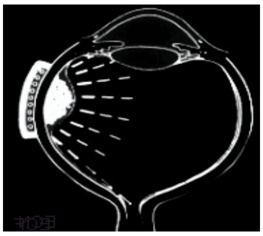


Fig 2.2.a.3. Surface eye plaque.

- Intraluminal: Sources are inserted into a lumen inside the lung as shown in Figure 2.2.a.4.

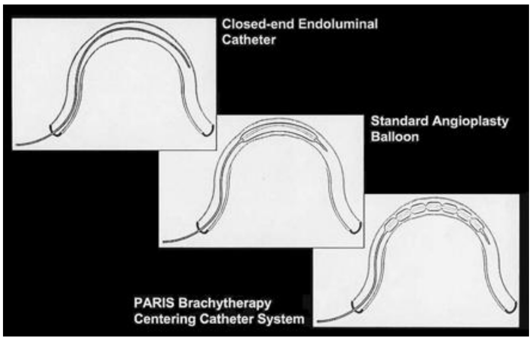


Fig 2.2.a.4. Fluoroscopy image shows centering balloon catheter introduced into transjugular intrahepatic portosystemic shunt.
Image taken from (http://www.ajronline.org/cgi/content/full/186/4/1133).

- Intravascular: A single source is placed into small or large arteries as shown in Figure 2.2.a.5. Intravascular brachytherapy is given immediately after balloon angioplasty is performed.

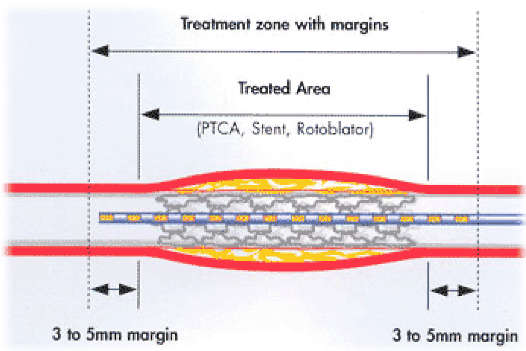


Fig 2.2.a.5. Intravascular brachytherapy treatment.

Image taken from (http://rahradiationoncology.com/serv-ivb.htm).

2.2.b Brachytherapy Treatments with regard to the Dose Rate

- Low dose rate (LDR); between 0.4 Gy/h to 2 Gy/h.
- Medium dose rate (MDR); between 2 Gy/h to 12 Gy/h.
- High dose rate (HDR); greater than 12 Gy/h (Suntharalingam, et al, 2006).

2.2.c Brachytherapy Treatments with respect to Source Loading

- Hot-loading: The applicator is pre-loaded and contains radioactive sources at time of placement into the patient. This is mostly used with LDR treatments as in eye plaque.
- After-loading: The applicator is placed first into the patient and the radioactive sources are loaded later, either manually or remotely by machine. This is used with HDR treatments. Figure 2.2.c.1 shows both manual and remote after-loading.



Fig 2.2.c.1 Manual after-loading and automatic remote after-loading.

Images taken from (http://www-naweb.iaea.org/nahu/dmrp/pdf_files/slides/Ch_13_MacForm.pdf).

2.3 Photon Source Characteristics and Practical Considerations

The radioisotope under consideration in this work, namely I-125, is classified as a photon emitter. In this section, some characteristics of photon emitter sources are presented, with some practical considerations related to brachytherapy cancer treatments.

2.3.a The Important Aspects of Any Brachytherapy Treatment

The important aspects of any brachytherapy treatment are the following:

- Using a suitable dosimetric model for the treatment time (Suntharalingam, et al., 2006). Since without an appropriate model that accounts for the complicated dosimetry of the encapsulated sources, accurate treatment planning cannot be achieved. This is where most of the work is currently done for the improvement of brachytherapy treatment. Objectives of our work fall under this category. We are dealing with the improvement of the dosimetric model of a particular brachy source.
- Use of calibrated sources with the calibration traceable to a standard laboratory. For that to be achieved, the most updated data about brachytherapy radioisotopes should be used in the dose calculations, before starting any brachytherapy cancer treatment. This facilitates having more accurate treatment planning, which leads in turn to more satisfactory clinical outcomes.
- Accurate source positioning allows for intense dose to be received by the localized target tumors, and protecting other healthy neighbor cells.

2.3.b Capsule Benefits of Encapsulated Brachytherapy Sources

Brachytherapy sources are commonly used as sealed sources, usually doubly encapsulated. The capsule serves multiple purposes; it absorbs alpha and beta radiation produced through source decay, in addition to providing the required rigidity of the source (Suntharalingam, et al., 2006).

2.3.c Useful Radiation Produced in Brachytherapy Sources

The different useful types of radiation that could be produced in brachytherapy sources are:

- Gamma rays.
- Characteristic x-rays resulting from electron capture or internal conversion that occurs in the source.
- Characteristic x-rays and Bremsstrahlung originating in the source capsule (Suntharalingam, et al., 2006).

2.3.d The Choice of the Radioisotope

The choice of an appropriate photon emitting radioisotope for a specific brachytherapy treatment depends on some physical and dosimetric characteristics. Examples are photon energy of the brachytherapy source, half value layer (HVL), specific activity, fall-off of dose with distance from the source, and the source half-life (Suntharalingam, et al., 2006).

2.4 Physics of Brachytherapy

The detailed and comprehensive physics of brachytherapy can be implemented in order to increase the accuracy of dose rate measurements, to improve the calculation formalisms, and to enhance methodologies used to evaluate or plan brachytherapy cancer treatment. This understanding is therefore essential to achieve better clinical outcomes. In this context, this work aims at implementing the physics of brachytherapy by Monte Carlo simulations. We will assess Task Group No. 43 protocol published by the American Association of Physicists in Medicine (AAPM).

2.4.a Task Group No. 43 Protocol

AAPM published Task Group No. 43 (TG-43) report in 1995 (Nath R., et al., 1995) in order to improve dosimetry methodologies and dosimetric characterization of commercially available brachytherapy source models. This was later updated in 2004 (Rivard, et al., 2004).

Previous calculation formalisms for radioisotopes were dependent on the apparent activity (in Ci or the equivalent-mass of radium). Therefore, these formalisms lack information on the energy emitted, and hence on the expected absorbed dose. The exposure rate constant was considered in air, which did not therefore take into account the effect of tissue. In addition, this old formalism did not take into account the manufacturing variations from one seed type to the other.

In contrast, the TG-43 generalized calculation formalism gives the absorbed dose rate in (cGy/h) at any point in tissue. Eq. 1 and Table 2.4.a.1 illustrate the dose rate formalism (Rivard, et al., 2004). Figure 2.4.a.1 depicts the coordinate system used for brachytherapy dosimetry calculations.

$$\dot{D}(r,\theta) = S_K \cdot \Lambda \cdot \frac{G_L(r,\theta)}{G_L(r_0,\theta_0)} \cdot g_L(r) \cdot F(r,\theta) \quad (1)$$

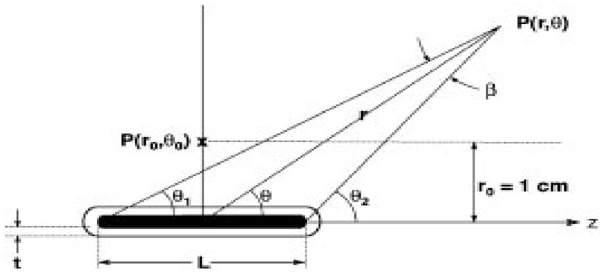


Fig 2.4.a.1 Coordinate system used for brachytherapy dosimetry calculations.

Table 2.4.a.1 Terms of the dose rate formalism (Eq. 1).

r	The distance (cm) from the origin to the point of interest P.
θ	The polar angle specifying the point of interest relative to the source longitudinal axis.
θ_o	The reference angle defines the source transverse plane and is equal to π/2 radians.
β	the angle, in radians, subtended by the tips of the hypothetical line source with respect to the calculation point, P(r, θ).
r_0	The reference distance and is equal to 1 cm.
S_K	The air kerma strength of the source ($\mu Gy.m^2.h^{-1}$) (1 U ≡ $\mu Gy.m^2.h^{-1}$) $S_K = \dot{K}_\delta$ (d) d^2, $\dot{K}_\delta$(d) is the air-kerma rate in vacuum, d is the distance from the source center to the point of $\dot{K}_\delta$ (d) specification.
Λ	The dose rate constant in water (cGy h^{-1} U^{-1}) The ratio of dose rate at the reference position, P (r_0, θ_0), and S_K $$\Lambda = \frac{\dot{d}(r_0,\theta_0)}{S_K}$$
G(r,θ)	The geometry function**:** an effective inverse square law correction based upon an approximate model of the spatial distribution of radioactivity within the source excluding photon attenuation.
g(r)	The radial dose function: describes the dose fall-off on the transverse plane due to photon attenuation**.**
F(r,θ)	The anisotropy function: describes the variation in dose as a function of polar angle relative to the transverse plane due to photon attenuation**.**
L	The length of the radioactive source (mm).
t	The thickness of the capsule (mm).

According to Eq.1, the formalism depends on the air kerma strength, S_K, and on the dose rate constant, Λ (Khan, 2003); both are measurable quantities that give directly the dose rate in tissue. In another contrast with the old formalism, the TG-43 calculation model takes into account the distribution of radioactivity inside the seed itself, as reflected by the unitless quantities g(r) and F(r,θ).

The geometry function, according to TG-43, is defined for a point source "*P*", or for a line source "*L*".

$$G_P(r,\Theta) = r^{-2} \, ,$$

$$G_L(r,\theta) = \begin{cases} \dfrac{\beta}{Lr\sin\theta} & \text{If } \theta \neq 0^{o} \\ \dfrac{1}{r^2 - L^2/4} & \text{If } \theta = 0^{o} \end{cases} \tag{2}$$

The radial dose function, g(r), accounts for dose fall-off on the transverse plane due to photon attenuation, *i.e.* excluding fall-off considered in the geometry function. The function g(r) is defined by Eq. 3, and is equal to unity at r_0= 1cm.

$$g_X(r) = \frac{\dot{D}(r,\theta_0)}{\dot{D}(r_0,\theta_0)} \; \frac{G_X(r_{0,}\theta_0)}{G_X(r,\theta_0)}. \tag{3}$$

The subscript ‘‘*X*’’ to the radial dose function and geometry function is intended to indicate whether a point source ‘‘*P*’’, or line source ‘‘*L*’’, is used in transforming the data.

The anisotropy function F(r,θ) (Eq. 4) describes the variation in dose as a function of polar angle relative to the transverse plane. While F(r,θ) on the transverse plane is defined as unity, the value of F(r,θ) off the transverse plane typically decreases as r decreases.

$$F(r,\theta) = \frac{\dot{D}(r,\theta)}{\dot{D}(r,\theta_0)} \; \frac{G_L(r,\theta_0)}{G_L(r,\theta)} \tag{4}$$

2.5 Objectives

Our work is basically aiming at the calculation, through MC simulation, of g(r) and the F(r,θ) parameters. These two parameters are design-dependent and can greatly vary according to the characteristics of the I-125 source (Figure 2.5.1).

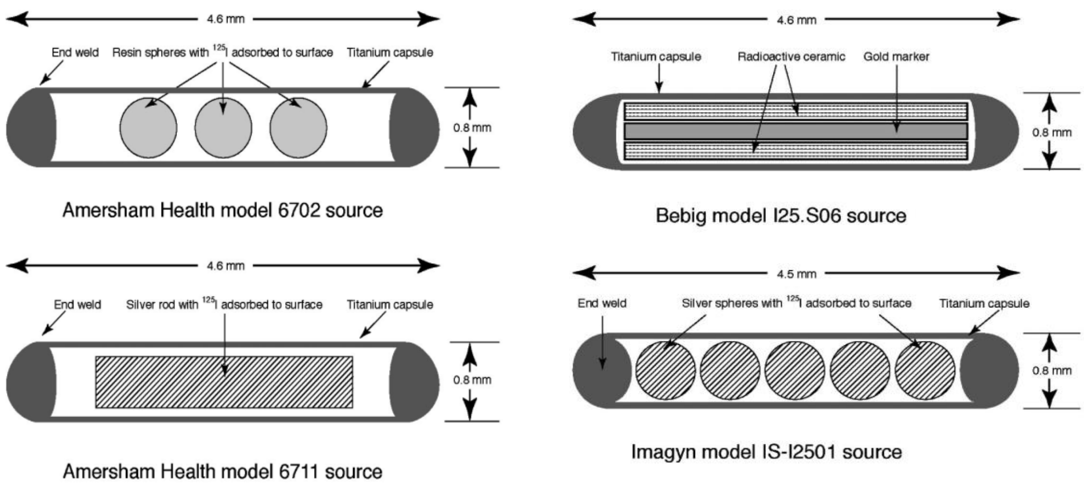


Fig.2.5.1 Some I-125 brachytherapy commercial seed models.

In this work, we consider seed type I25.S06 source from Bebig, Germany (Rivard, et al., 2004). This is the source design used in brachytherapy application at the King Hussein Cancer Center.

We will follow the following procedure:

1. Finding g(r) for I-125 point source.
2. Finding g(r) for a pure I-125 line source.
3. Building real geometry for our seed Bebig model I25.S06.
4. Finding g(r) for the actual I-125 line source for our seed, Bebig model I25.S06.
5. Finding F(r,θ) for our seed, Bebig model I25.S06.

Each seed contains a cylindrically shaped ceramic, saturated with radioactive iodine-125 compound, and enclosed in a laser-sealed titanium tube. A gold wire inside the ceramic is used as an X-ray marker.

The details of the seed geometry as modeled in this work follow Heintz, et al., (2001) and are listed in Table 2.5.1.

Table 2.5.1 Physical characteristics of the considered seed with the internal design of the cylinder.

Source marketing company	Uro med
Source manufacturing company	Bebig GmbH
Source model name	I25.S06
Manufacturing location	Germany
External length	4.5 mm
External diameter	0.8 mm
Wall thickness	0.05 mm
End design	Laser welded (semi-circle)
End thickness	0.44-0.48 mm
Internal design type	Cylinder /rod
Rod/wire/cylinder length	3.5 mm
Rod/wire/cylinder	Ceramic cylinder
Outer diameter	0.6 mm
Inner diameter	0.22 mm
Marker type	Gold marker
Marker diameter	0.17 mm
Internal design construction	^{125}I radioactive ceramic cylindrical shell gold marker (rod) inside the ceramic cylinder
Radiographic marker	gold rod
Minimum source strength	0.203 mCi
Maximum source strength	0.634 mCi

2.6 Iodine-125

The iodine radioisotope I-125 has a half-life of 60 days. It decays as a result of electron capture to excited state of Te-125, followed by X-rays and γ-radiation in the energy range up to 35 keV. The average weighted energy is 28 keV. Figure 2.6.1 shows the I-125 decay scheme. Considering the encapsulated actual brachytherapy source I25.S06 Bebig model, the electrons emitted during this decay are absorbed in the titanium capsule material (BEBIG Vendor, 1999).

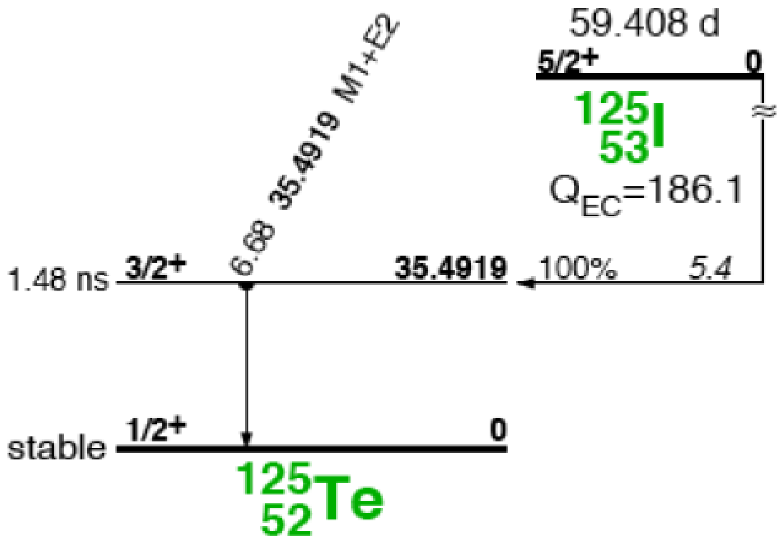


Fig 2.6.1 The I-125 radionuclide decay (Ravinder, 2005).

CHAPTER THREE
SIMULATION

3.1 Computer Modeling and Simulation

The use of experimental methods in brachytherapy is complicated because of the high dose gradient at short distances. This necessitates using a high resolution detector. In addition, the emission of low energy photons makes the detector composition and its characteristics very critical (Calatayud, et al., 2009). Among those characteristics are linearity of response with dose, spatial resolution, energy dependence and influence of positioning.

As a result, virtual experiments, also known as computer modeling and simulation, recently found wide application not only for resolving those concerns, but also for testing proposed experimental setups before they are built.

The appropriate modeling code should take care of the detailed geometry of the system; the composition of its components in terms of dimensions, materials, physical state and density. The simulation itself follows the modeling of the geometry. It applies all the different and relevant physics processes of the interaction of radiation with matter.

3.2 Monte Carlo Methods

Monte Carlo (MC) method is a problem solving tool that uses stochastic approach, *e.g.* based on random numbers, to simulate the interaction of radiation with matter. Due to this stochastic approach, MC is also used in other probability-based calculations such as risk analysis in nuclear facilities and other fields, the stock market, economics, and even the estimation of the traffic flow. The use of MC methods to simulate physical problems became popular, as it allows the examination of more complex systems than can either be described analytically, or measured experimentally.

The following toolkits and codes are examples for the application of MC to simulate physics related to medicine: EGSnrc, MCNP, PENELOPE, FLUKA, and GEANT4. For our work we have opted to use GEANT4.

3.3 GEANT4

GEANT4 is a platform for simulation using Monte Carlo methods. It is a comprehensive toolkit dedicated for the simulation of the passage of particles through matter. It requires basic knowledge of object oriented programming using C++. GEANT4 was originally developed for high energy physics. Nevertheless, applications now include nuclear, space and medical physics among others. Medical applications include characterizing machines and sources, calculating dose and the development of imaging technology.

The source code and libraries are available freely at the project web site. GEANT4 finds use in medical physics because of its ability to handle very complex geometry and to handle all particles with detailed tracking and interactions.

3.3.a GEANT4 Features

GEANT4 includes facilities for handling geometry, tracking, detector response, run management, visualization and user interface. For many physics simulations, this means less time that needs to be spent on the low level details and researchers can start immediately on the more important aspects of the simulation.

Following is a summary of each of the facilities mentioned above:

- Geometry: is an analysis of the physical layout of the experiment, including detectors, absorbers, and other components. It takes into consideration how this layout will affect the path of particles in the experiment.
- Tracking: means simulating the passage of a particle through matter. This involves considering possible interactions and decay processes. The simulation

follows the primary particle and all the secondary particles that are emitted from each interaction site and records interaction types and energy transferred. The simulation continues to follow each particle until certain conditions occur. In our work, the simulation continues in following up photons and their possible interactions which produce electrons. These secondary electrons are also tracked. There is a cut value, however, of energy range which is less than the voxel width.

- Detector response: is recording when a particle passes through the volume of a detector, and how much energy was transferred.
- Run management: is recording the details of each run (a set of events), as well as setting up the experiment in different configurations between runs (http://en.wikipedia.org/wiki/Geant4).

3.3.b GEANT4 in Medical Physics

After the recognition of MC as an alternative to experimental methods, GEANT4 medical applications have been significantly increased.

GEANT4 could be used for all types of particles, while some other codes like EGSnrc is applicable only for electrons and gammas. GEANT4 could model all types of geometry no matter how complex they are.

Simulation in medical physics could be fruitful for characterizing beams and brachytherapy sources, treatment planning, retrospective studies, imaging and validation.

Medical physics applications do involve relatively complex geometries, such as the photon intensity modulated radiotherapy (IMRT), multileaf collimators (MLCs) and brachytherapy sources in a catheter (Perl, 2007).

Another aspect of GEANT4 is the ability to handle fields, both electric and magnetic. The toolkit incorporates also experimental setup visualization, with very simple user interfaces. Most importantly, comprehensive physics processes are included in the toolkit.

It should be noted that GEANT4 is not a plug and play code; the user has to build his own code that is specific to the question being investigated. Proper code building is essential to the accuracy of the results.

3.4 Root

Root is an object oriented framework program and library developed by CERN. It was originally designed for particle physics data analysis and contains several features specific to this field. Nevertheless, it is also commonly used in other applications such as nuclear physics, nuclear astrophysics, astronomy and data mining. It aims at solving the data analysis challenges the physicists meet in many disciplines.

3.4.a Advantages of the Framework

The benefits of ROOT can be summarized as follows (Root User Guide, 2008):

- Less code to write: the programmer should be able to use and reuse the majority of the existing codes. Basic functionality, such as fitting and histogramming are implemented and ready to use and customized.
- Codes inherited from other frameworks have already been tested and integrated with the rest of the framework.
- It makes it easier to break programs into smaller pieces.
- More focus on areas of expertise: users can concentrate on their particular problem domain. They do not have to be experts at writing user interfaces,

graphics, or networking to use the frameworks that provide those services. They have to write the code that deals only with their specific needs.

3.5 Why MC Simulation in this Research

The aim of our work is to characterize the dosimetric parameters of an actual design of a radioactive seed that is used clinically. The complex designs and the cascade of various particles emitted from the source, together with the source encapsulation, beta, gamma and x-rays emitted, make analytical equations very complex and prone to erroneous approximations.

In addition, and as mentioned at the beginning of this chapter, measurement experiments for brachytherapy sources are complicated. This implies that the use of MC simulations in a "virtual experiment" is the most practical and accurate method to-date.

3.6 Codes of Our Work

In this work, we wrote some new codes for data analysis and for geometry modeling of the source. We modified other codes related to simulation, each serves a certain purpose. Some of these codes will be presented in the following sections, listed according to the research approach sequence, with a description of the specific role of the code.

Measurement simulation codes are designed to register the deposited energy in the entire phantom voxels. Figure 3.6.1 shows the voxels in a water phantom box. While data analysis codes are those that are responsible for selecting certain voxels with their energy deposition, according to requirements and conditions that are specified in the code. The analysis codes serve other purposes like drawing histograms and contours.

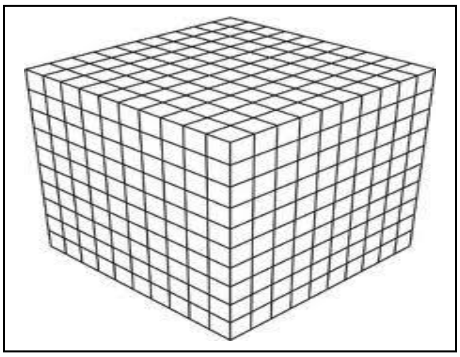


Fig 3.6.1. Water phantom box voxels.

The execution of any code, whether it was a measurement or data analysis code, is called a run. Each run provides final results in an output file.

The runs in our work were repeated more than sixty times delivering sixty output files. The output files are merged to provide one output file through two steps: The first step was writing a code to sum measured deposited energy for each voxel in that file, since there are multiple energy deposition in each voxel during a run. The second step was writing a code to sum energy deposition for each voxel for all runs.

Those multiple and long runs described above serve to improve statistics by generating a large number of primary events.

3.7 Validation

As mentioned earlier, GEANT4 is a toolkit that enables the user to build his own codes for the particular setup and experiment. As such, every code that is written for this work has to be validated. The following validations were performed:

a. Material validation.

b. I-125 decay spectrum validation.

c. Dose fall-off validation.

d. The visualized actual seed design.

e. The geometry validation.

3.7.a Material Validation

For each material, such as water, the user has to write a piece of code that includes information such as the elements composing the material, their fractional weight, as well as the density. To assure that the code has been written properly, it has to be validated.

The material validation was done by irradiating a block of that material with photons of known energies, tallying the transmitted photons, and then calculating the mass attenuation coefficient. Results were compared with published values of the coefficients.

3.7.b I-125 Decay Spectrum Validation

To ensure that the isotope simulated decay properties are properly representing the intended I-125, we wrote *count.c* code. It is a code that counts and histograms decay lines emitted by the isotope. These were then compared to published decay lines of I-125.

3.7.c Point Source Fall off Validation

The first step of our simulation work was to use I-125 in a point source configuration. The fall off of dose with distance was first verified. The normalized dose rate (normalized to the dose at 1 cm from the source) have been obtained using an analysis code called *graph.c*.

3.7.d The Visualization Validation

The visualization of the modeled geometry serves to qualitatively test the intended source and phantom structure. Though neither material nor dimensions can be verified in this step, but it is helpful for providing first insight on the modeling. This has to be complemented by more rigorous material and dimension (geometry) validation.

3.7.e The Geometry Validation

Geantino is a virtual non-reactive particle that travels in the specified direction, and gives, as an output, the volumes it meets and their locations. The geantino can be "fired" towards any direction and angle, and from the output of the geantino, one can verify that the geometry of the experiment is as required. The written geantino run code is flexible, and the direction of the fired geantino can be altered in order to comprehensively test the whole geometry.

For example, one code is called *cascade+Z.mac* for geantino fired along the positive z-axis, and the other one called *cascade-Y.mac* for fired geantino along the negative y-axis.

3.8 Characterization of I-125 Dose Parameters

For the characterization of dose parameters according to the TG43 formalism, two functions should be identified: The first is the geometry function $G(r,\theta)$ that has been calculated according to TG43 equations, for both point and line sources. The second will be dealt with in this work by MC simulations, and characterizes the two dose parameters, which are the radial dose function $g(r)$, and the anisotropy function $F(r,\theta)$.

This proposed policy of characterization for the I-125 dose parameters will be followed in our work for three different situations: the point source, the line source, and the actual real seed Bebig model I25.S06.

3.8.a I-125 Point Source

Due to the fact that radiation-emitting point sources are assumed to be isotropic in nature, the corresponding anisotropy function $F(r,\theta)$ is always equal to one, The only thing to be found is then the radial dose function $g(r)$. Correspondingly, codes have been written to perform the modeling and calculations. The primaries are generated using the macro *cascade.mac.*

The geometry function for the point source was calculated using $G(r,\theta) = 1/r^2$. For data analysis, two codes have been written: The first one sums the energy deposited in each voxel in one output file, and it is called *analysis-efficient.c*. The other code sums the deposited energy in all of the sixty output files for all runs, and it is called *multi-analysis-update.c*.

At the end, values of the radial dose function g(r) were calculated. The values were compared and contrasted with published results.

3.8.b I-125 Line Source

For the line source, both the radial dose function g(r), and the anisotropy function $F(r,\theta)$ could be found. We followed the same scheme of work described for the point source. The geometry function $G_L(r,\theta)$ was calculated according to Equation (2) in Chapter Two. The line source was an intermediate step between point source and actual seed design. It not only helps in formulating the different parameters needed in the logical transition to the actual seed, but in the development and validation of the written codes of this work as well.

New set of codes have been written. The corresponding macro code is *cascade.mac*. Data analysis codes are *analysis-efficient.c* to sum within one file, the other one is *multi-analysis-update.c* which sums energy deposition in each voxel for all sixty runs.

3.8.c Actual Seed Design

For the actual seed design, both the radial dose function g(r), and the anisotropy function F(r,θ) have been found. The same technique used for I-125 line source was applied, but with of course the actual source design (Bebig model I25.S06). The code written for building the actual seed geometry according to the vendor is called *detector construction.c*. The design follows Rivard, et al., (2004). Figure 3.8.c.1 depicts the seed design.

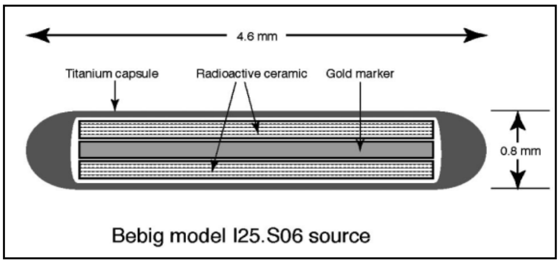


Fig 3.8.c.1 The I25.S06 Bebig model.

Correspondingly, the macro *cascade.mac* has been written to find the radial dose function g(r) for the actual seed design, the same data analysis codes written for the line source, and the same geometry function $G_L(r,\theta)$ values have been used.

In finding the anisotropy function F(r,θ), energy deposited at the centre of all voxels of the phantom should be registered. This is in contrast to finding g(r) which follows the y-axis only. This adds to the complication of these calculations. Even geometry function $G_L(r,\theta)$ calculations were conducted through simulation. For $G_L(r,\theta)$ calculations, a code named *GeometricEnergy.c* has been written.

Other data analysis codes have been also written. One code serves to sum energy deposition in each voxel within one file; it is called *analysis-geo-sum.c*. Another code sums the deposited energy in all of the sixty output files for all runs; it is called *multisum-analysis-geo.c*.

The final results of both g(r) and F(r,θ) were compared to published data and presented in Chapter Four.

CHAPTER FOUR

RESULTS AND ANALYSIS

In this chapter, we present the results of our work. However, since this is a simulation-based research, we always begin with the validation of the particular code that was built for every process.

4.1 Validation

The codes validation is the most important step in any simulation-based research. The codes that need to be validated here are those written or developed for our particular application, in addition to some relevant features of the general purpose toolkit itself i.e. GEANT4. Codes are responsible for modeling, measurements, data analysis and addressing simulation results according to the code demands. As such, codes validation is essential before any conclusions can be withdrawn from the output results.

4.1.a Material Validation

This validation is required to ensure that material definition used in the code is correct, and that the simulation is calling up the correct elements/materials. The material validations have been performed using a separate code dedicated for this purpose. Some modifications were done to cope with each material type. The method is based on finding out the mass attenuation coefficient (μ/ρ) as represented in Eq. 5. In order to find out the mass attenuation coefficient, we simulated various beams of gamma-rays incident on a known thickness of the material, and recorded the output intensity *I(x)*;

$$I(x) = I_o \, e^{-(\mu/\rho)\,\rho x} \,. \qquad (5)$$

While I is the transmitted intensity, I_0 is the incident intensity, X is the geometrical thickness of the material, ρ is the absorber mass density, and (μ/ρ) is the mass attenuation coefficient usually given in cm^2/g.

The mass attenuation coefficient for every material used was calculated, and the results were then compared to the NIST-XCOM standard published data (http://physics.nist.gov/PhysRefData/Xcom/Text/XCOM.html). The validations have been done for different values of photon energies, namely 30 keV, 100 keV, 200 keV, 300 keV, 400 keV, 500 keV and 1 MeV. The primary incident photon intensity I_o was either one million photons per run, or ten million if implied by the need for better statistics. We present below the results of material validation for photon energy 30 keV.

Table 4.1.a.1 lists the simulated mass attenuation coefficient results vs. the published XCOM data, together with the percent error. Materials listed are iodine, gold, titanium, and water that are relevant to our application. The percentage error values lie within the range of 0% - 0.12%. This shows that the first step of identifying the correct materials for our work is successful.

Table 4.1.a.1. Comparison of mass attenuation coefficients at 30 keV photons & 1 million primaries.

Material	Mass Attenuation Coefficients with Coherent Scattering (cm^2/g)		Percentage Error
	Simulated	Published XCOM	
Iodine	8.560	8.56	0%
Gold	27.47	27.5	0.11%
Titanium	4.964	4.97	0.12%
Water	0.3762	0.376	0.05%

4.1.b I-125 Decay Spectrum Validation

The purpose of this part is to assure that the code can properly reproduce the decay of I-125 radioisotopes. We began with two million I-125 primary particles and allowed them to decay. As an output, we recorded the different emissions of these radioisotopes and compared them with known emission data for both I-125 along with the transitions of its daughter Te-125. Figure 4.1.b.1 depicts the decay spectrum produced in the

simulation for this particular source. The figure was drawn using the *count.c* code developed in this work, as described in Chapter Three, namely section **3.7.b.**

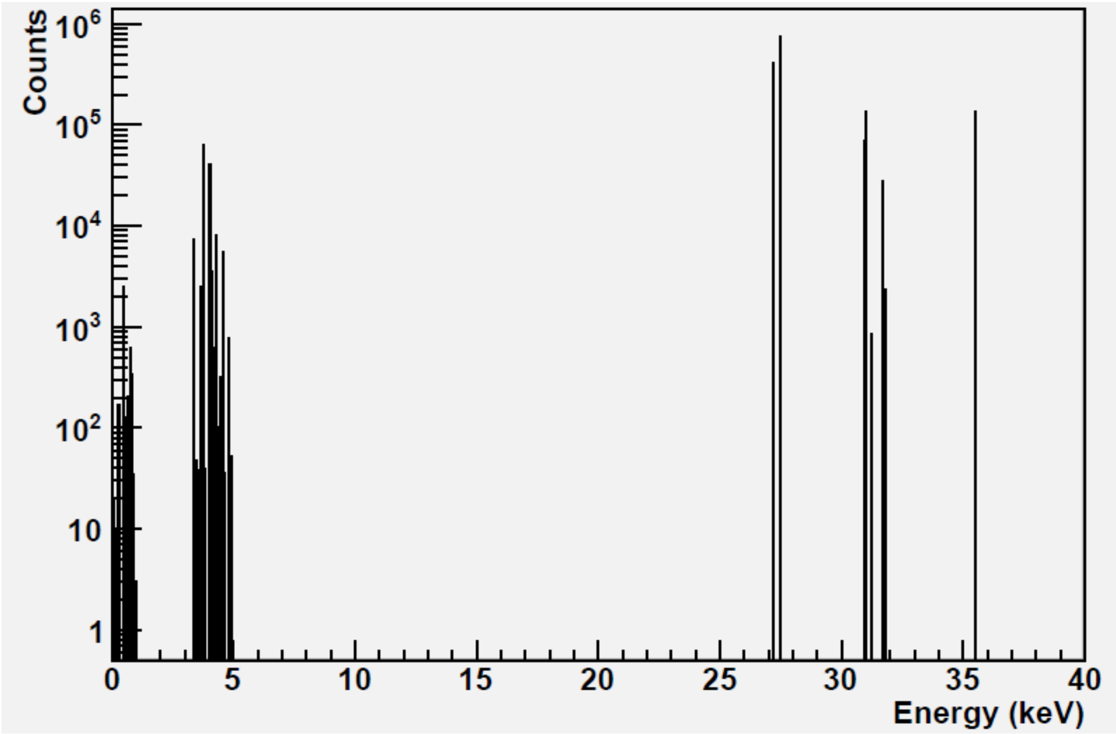


Fig 4.1.b.1: The I-125 radioactive source decay spectrum produced by simulation.

Table 4.1.b.1 shows the comparison between the spectrum lines as produced by the simulation and the reference data from the National Nuclear Data Center (NNDC) (http://www.nndc.bnl.gov/). The table shows a very good agreement between simulated and published intensities. Italic underlined energy entries shown in the table have slight differences between published and simulated intensities. This difference could be attributed to statistical errors that might decrease by increasing the number of primaries used in the simulation.

All in all, results show that the decay obtained through simulation does reproduce the I-125 radioisotope decay data. Hence, the objectives of decay validation have been achieved.

Table 4.1.b.1. Simulated vs. published I-125 energy lines and their corresponding intensities.

Simulated Energy (keV)	Simulated Intensity	Published NNDC Intensity
3.35	*0.003*	*0.001*
3.63	0.001	0.001
3.75	0.003	0.003
3.76	*0.03*	*0.01*
4.025	0.02	0.02
4.05	*0.0010*	*0.0019*
4.1	0.002	0.002
4.17	0.0003	0.0003
4.29	*0.0004*	*0.003*
4.57	*0.00275*	*0.0014*
4.865	0.000002	0.000002
27.19	0.202	0.202
27.47	0.376	0.376
30.94	0.035	0.035
30.995	0.067	0.067
31.215	0.0003	0.0003
31.685	0.014	0.014
31.755	0.000056	0.000052
35.495	0.067	0.067

4.1.c Dose Fall-off Validation

A step further in our code development was aimed at scoring dose along various directions from the source. We started with a simple case, the point source, for which we wrote a code to score the dose radially outward. The point source was, in fact, a sphere of radius 0.01 mm placed in the water phantom. Figure 4.1.c.1 depicts the point source dose fall-off with distance r compared to the mathematical inverse square law.

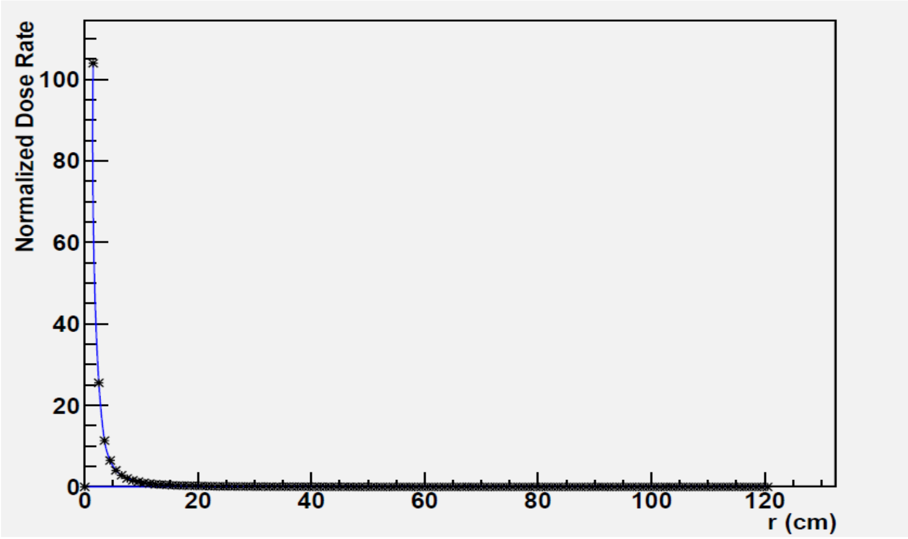


Fig 4.1.c.1. The simulated normalized dose fall-off (data points). The inverse square law is depicted by the curve.

For a closer look at the simulated data, the dose rate fall-off has been drawn on a semi-log graph. The dose rate was normalized to the corresponding value at 1.0 cm, and compared to the mathematical *$1/r^2$* behavior. This is presented in Figure 4.1.c.2.

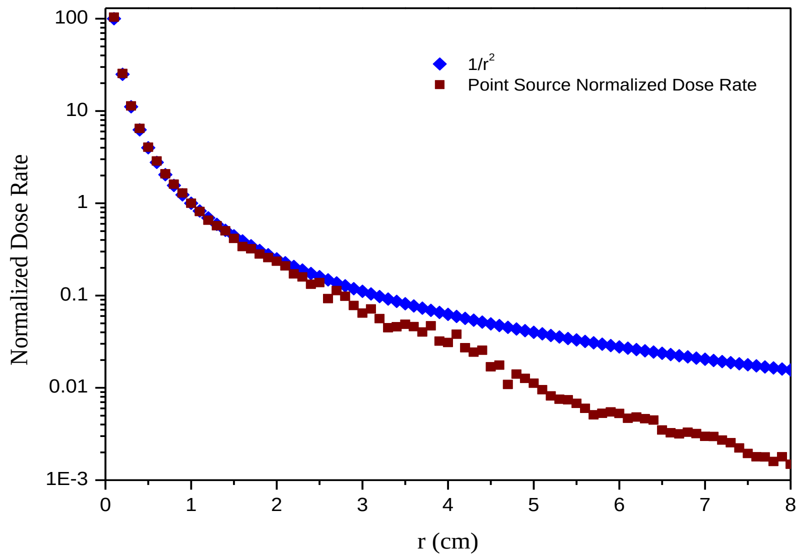


Fig 4.1.c.2: The normalized simulated dose rate versus *$1/r^2$* on a semi-log scale.

It is noted that, while the dose rate is falling off per inverse square relation closer to the point source, the attenuation in water leads to deviation from the pure mathematical behavior at larger distances.

The effect of medium attenuation on the absorbed dose at any radial distance, with the inverse-square behavior excluded, is the dosimetric parameter known as the radial dose function, *g(r)*. This function has been defined earlier in Chapter Two, namely in Section 2.4.a.

On the other hand, and as expected, the radial dose fall-off for the line source is different from that for the point source. Mathematically, the inverse-square component in the dose fall-off does not apply. In addition, overall medium attenuation preceding a given location in the phantom depends on this linear geometry. Figure 4.1.c.3 shows the radial dose fall-off away from a point source compared to the corresponding behavior for the actual seed. The $1/r^2$ component is shown as well.

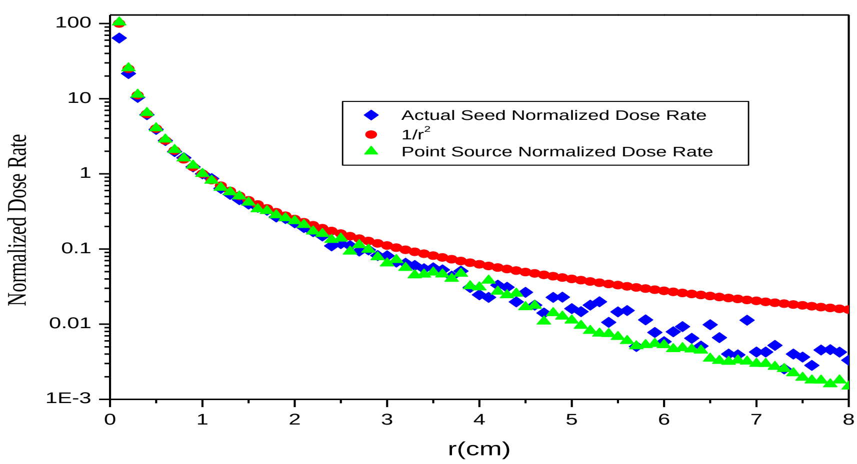


Fig 4.1.c.3: The normalized simulated dose rate (log. scale) vs. distance *r* for point and actual seed.

For the actual seed design, the fall-off of dose is complicated by the distribution of radioactivity inside the capsule itself, and the various materials used in the encapsulation. Figure 4.1.c.3 shows that the dose fall-off for the actual seed is shallower than that for the point source. This can be attributed to the edges of the source which contribute to the radial dose by primary and scattered photons. We also notice that the data for the actual seed is "noisier" than that of the point source due to photon attenuation that occurs inside the capsule itself. The effect of radioactivity distribution

inside the capsule, and of the capsule material, are studied in Section 4.2 as the characteristics of the dose parameters, which are the radial dose function *g(r)* and the anisotropy function $F(r,\theta)$.

4.1.d The Visualized Actual Seed Design

As mentioned previously in Chapter Three, it is important to visualize the modeled geometry as a preliminary test before applying the geantino test. The process of visualization can also optionally include tracking of small number of primary and secondary particles. The test was applied to point and line sources, as well as for the actual seed design.

For the purpose of simulation, the point source is modeled as a sphere with radius equals to 0.01 mm. The visualization of the point source itself is trivial, but the tracking of particles emitted from the source is worth to be considered. The line source has been visualized as well. For building the actual capsule geometry, we referred to TG-43 (Rivard, et al., 2004) and Heintz, et al. (2001); both reported detailed geometrical and material design description of I-125 model I25.S06 source from Bebig.

Figures 4.1.d.1 and 4.1.d.2 depict the visualization of the I-125 line source, and the Bebig actual model, respectively.

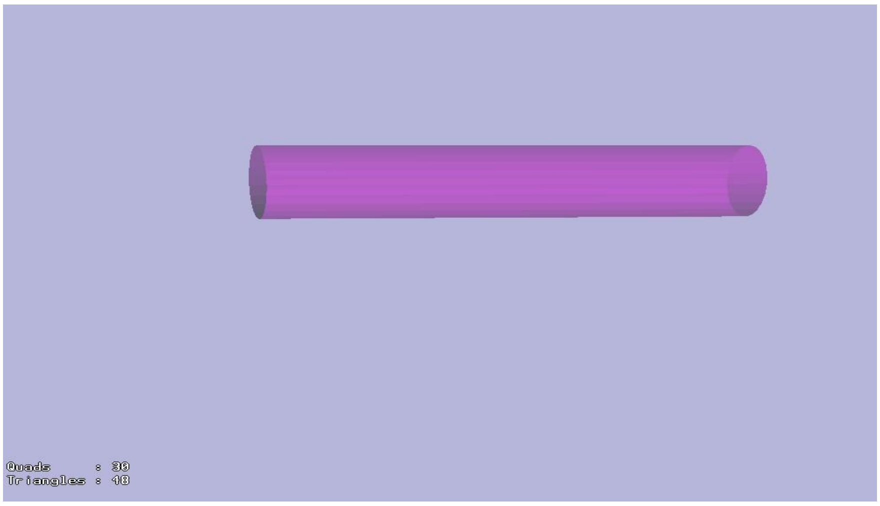


Fig 4.1.d.1: The visualization of the I-25 line source.

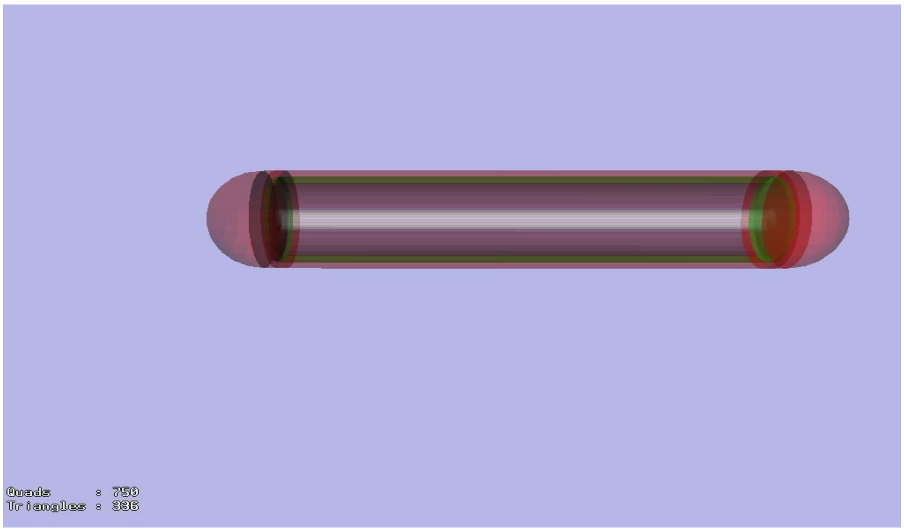


Fig 4.1.d.2: The visualization of the actual Bebig seed.

Figure 4.1.d.2, when qualitatively compared to Figs. 4.1.d.3 and 4.1.d.4, illustrate that the modeling code reproduces the real seed design. Needless to say, quantitative validation of dimensions and materials has been also performed in order to complement this preliminary test (Sections 4.1.a and 4.1.e).

The capsule is made of I-125 embedded in ceramic, a gold marker lies at the central part of the capsule. This gold marker is used by medical doctors to visualize, by x-ray imaging, the orientation of the seed inside the patient. Both ends of the capsule is welded with Titanium.

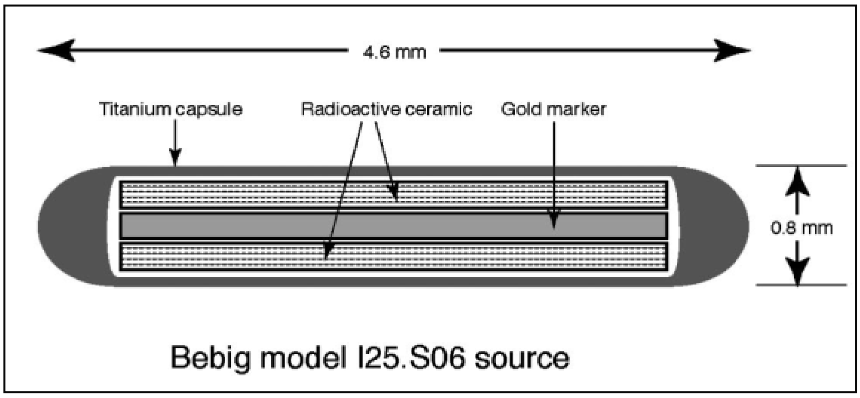


Fig 4.1.d.3: The actual seed design I25.S06 Bebig model (Rivard, et al., 2004).

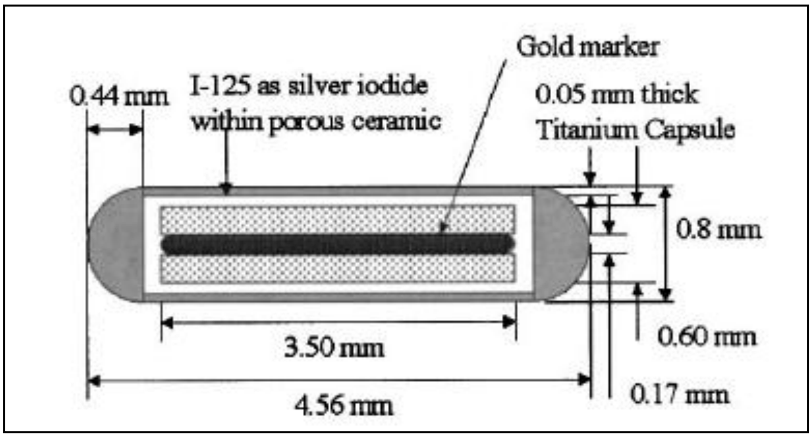


Fig 4.1.d.4: The actual seed design I25.S06 Bebig model (Heintz, et al., 2001).

4.1.e The Geometry Validation

The preliminary and qualitative visualization described above has to be complemented by material validation (Section 4.1.a), in addition to a quantitative test of dimensions. The relatively complex geometrical details of the capsule, with all the various structures inside as illustrated in Figures 4.1.d.3 4.1.d.4, have to be accurately modeled and verified.

The center of the source is placed at global coordinates (x, y, z) = (0.5 mm, 0.5 mm, 0.5 mm); whereas the phantom center at (0, 0, 0). This arrangement was designed in order to facilitate measuring the deposited energy recorded at the center of each voxel, which in this case is at full integer distance from the center of the source.

To verify that the proper physical volume is placed in its proper location, we have to do geometry validation. For this purpose, we used the so called geantino particle. The geantino traverses the material without interaction; it reports back, as output, the volumes it encounters with the corresponding (x, y, z) coordinates.

The geantino particle was launched from the phantom's point of origin. In our work, many geantino tests have been done along different directions. In order for the output to be readable by the user, it is essential to know the name of each physical volume in the

geometry modeling, and what does it represents. Table4.1.e.1 presents an example of geantino test results along +z-axis. Results confirmed that the geometry was accurately modeled, and exactly reproduces the actual source model.

Table 4.1.e.1: Geantino test results along +z-axis.

G4Track Information:	Particle = geantino,		Track ID= 1,		ParentID = 0
X(mm)	Y(mm)	Z(mm)	StepLeng	TrackL	NextVolume ProcName
0.5	0.5	0.5	0	0	MarkerPhys initStep
0.5	0.5	2.25	1.75	1.7	capsule2Phys
0.5	0.5	2.27	0.02	1.77	Capsule5Phys
0.5	0.5	2.35	0.08	1.85	CapsuleTip1IodiumPhys
0.5	0.5	2.75	0.4	2.25	PhantomPhys
0.5	0.5	150	147	150	WorldPhys

4.2 Characterization of I-125 Dose Parameters

Section 4.1 dealt with the validation of the codes developed in this work in order to verify that the materials, I-125 decay, source model and dose rate in water are accurately accounted for.

From this section onward, we will be addressing the objectives of our work; *i.e.* the I-125 characterization of dose parameters for point source, line source, and for the actual Bebig model I25.S06 seed design.

4.2.a I-125 Point Source

Since the dose from the I-125 point source is conceptually isotropic, the anisotropy function $F(r,\theta)$ is constant and equals to one. The only dosimetric parameter required for the point source is thus the radial dose function, $g(r)$, given by Eq. 3 in Chapter Two, and plotted along the y-axis from 0.5 - 10 cm from the center of the source. Values of x and z were therefore fixed at the source center (Figure 4.2.a.1).

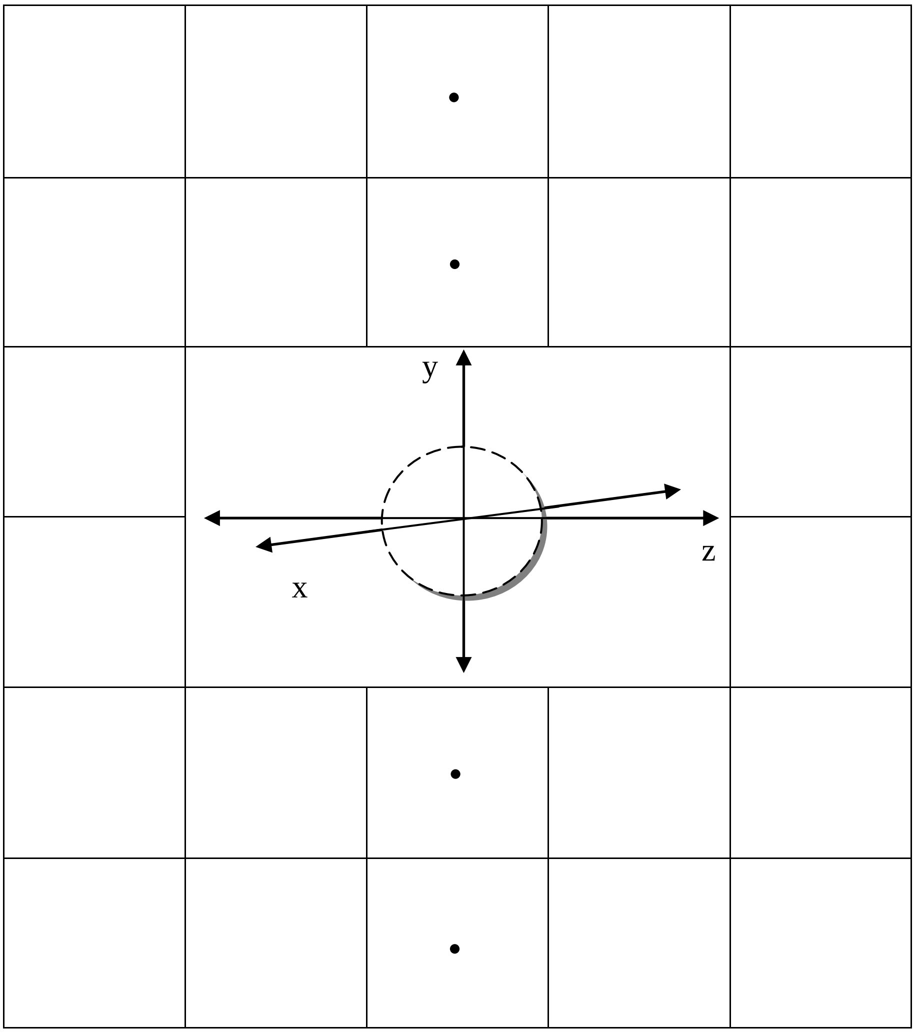


Fig 4.2.a.1. Water phantom voxels for point source *g(r)* measurement at the center of each voxel along the *y*-axis.

The simulated *g(r)* values were found cumulatively from 60 simulation runs. Each run was performed with 5 million I-125 primaries. The results are presented in Table 4.2.a.1 and depicted in Figure 4.2.a.2, labeled as “Simulated GEANT4”, and compared to other published values. At 0.5 cm, our results are larger than the corresponding values in both references. Nevertheless, at far distances, our results become lower.

Table 4.2.a.1. Comparison between simulated and published *g(r)* data for I-125 point source. The values are normalized to the corresponding value at *y* = r = 1 cm.

r (cm)	TG-43 (Rivard, et al., 2004)	EGSnrc (Taylor & Rogers, 2008)	Simulated GEANT4 (This work)
0.5	1.001	1.009	1.07943
1	1	1.002	1
1.5	0.942	0.941	0.91212
2	0.863	0.863	0.90549
3	0.695	0.699	0.62032
4	0.543	0.55	0.52227
5	0.413	0.417	0.26908
6	0.316	0.317	0.17907
7	0.234	0.24	0.1443
8	0.178	0.18	0.09827
9	0.135	0.133	0.06207
10	0.0967	0.0975	0.05204

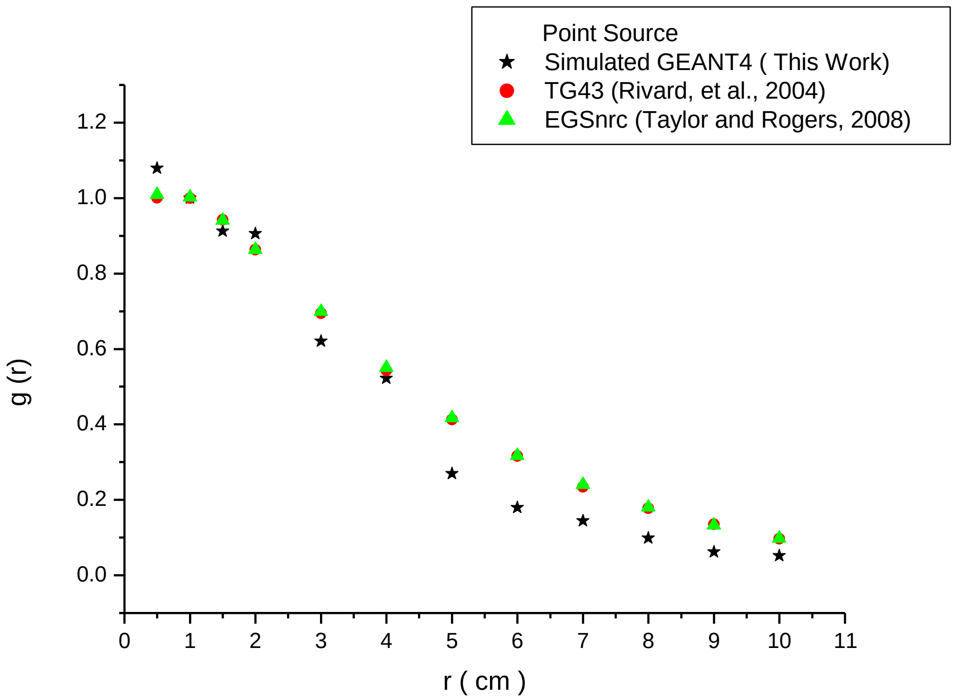


Fig 4.2.a.2.The simulated and published values of radial dose function *g(r)* for point source.

Taylor and Rogers (2008) used EGSnrc MC code. The purpose of their work was to reproduce TG-43 values in order to find a better fitting equation. However, this means that they had to suppress electron transport in water. In addition, they did not follow photons with energies less than 1 keV. Quoting from their paper:–"Electrons are not

transported and photons are transported until their energy falls below 1 keV" (Taylor & Rogers, 2008). By suppressing electron transport, two things occur artificially:

1. Electrons generated from the source, such as Auger electrons, are not transported to the medium. As such, the g(r) at 5 mm, as calculated by Taylor & Rogers (2008) is 7% lower than the value in our work, namely 1.001 vs. 1.079, respectively. In contrast, by allowing the code to follow the electrons in their natural path of interaction, we found higher doses in the near vicinity of the source.
2. Electrons that are produced by photon interactions in the water medium in their work, are not transported, and their energy is forced to be deposited locally. As such, the *g(r)* values at distances further away from the source are higher. In our work, we allowed the code to track the electrons as they travelled through the medium. As each electron is created, it deposits its energy in small increments along its path. This is illustrated as smaller values of *g(r)*.

The above restrictions imposed on electron transport by Taylor & Rogers (2008) was good for the objectives of their work; namely to reproduce TG-43 values and find a better fit. Our objective is to improve the accuracy of the dosimetric values, as such, no restrictions on electron or photon transport was imposed on the code. Our GEANT4 MC comprehensively tracks the interactions of all photons and electrons emitted by I-125 and its daughter, as well as it follows the electrons that are produced by the primaries in the phantom.

Looking at TG-43, we find that for closer distances to the source, the values used are either interpolated or non-consensus (Rivard, et al., 2004).

Based on the above, we propose that our result of *g(r)* is more accurate than both TG-43 and the work by Taylor & Rogers, (2008). Nevertheless, we need to acquire better statistics.

In order to make *g(r)* values more handy, we used a fifth order polynomial (Eq. 5) in order to fit our results.

$$g(r) = a_0 + a_1 r + a_2 r^2 + a_3 r^3 + a_4 r^4 + a_5 r^5. \qquad (5)$$

The fitting parameters are listed in Table 4.2.a.2.

Table 4.2.a.2: Fitting parameters for *g(r)* of the point source.

Fitting Parameter	Value
a_0	+1.09571
a_1	-2.428×10^{-2}
a_2	-6.623×10^{-2}
a_3	$+9.67\times10^{-3}$
a_4	-3.17825×10^{-4}
a_5	-6.676777×10^{-6}

On the other hand, Table 4.2.a.3 presents a comparison between our simulated and fitted results of *g(r)*. The percentage difference ranges between 1% and 24%.

Table 4.2.a.3. Comparison between simulated and fitted *g(r)* results for I-125 point source.

r (cm)	Fitted Simulated GEANT4 (This work)	Simulated GEANT4 (This work)	Percentage Difference %
0.5	1.0682	1.07943	1.04
1	1.01455	1	1.45
1.5	0.94125	0.91212	3.19
2	0.85429	0.90549	5.65
3	0.6605	0.62032	6.48
4	0.4695	0.52227	10.10
5	0.30752	0.26908	14.28
6	0.18994	0.17907	6.07
7	0.12045	0.14430	16.53
8	0.09021	0.09827	8.20
9	0.07711	0.06207	24.23
10	0.04488	0.05204	13.76

4.2.b I-125 Pure Line Source

Since we are migrating from point source into the actual seed design, it was important for our work to verify our codes in an intermediate step; *i.e.* by building a pure I-125 line source. The data from this section is roughly compared to the published data of actual line sources. Naturally, the results are not expected to be identical. However, the comparison is only meant to demonstrate that the code handling the line geometry is well written.

In this section, we again present the radial dose function *g(r)*. As a reminder to the reader, the *g(r)* is the normalized dose rate with the geometry effect excluded (compare Eq. 3 in Chapter Two). For the point source, the geometry function, $G(r,\theta)$, is the simple $1/r^2$. However, for a line source it is given by Eq. 2 of Chapter Two. For every distance, *r*, we wrote a code to calculate $\frac{G_L(r_0,\theta_0)}{G_L(r,\theta_0)}$, where r_0 = 1 cm and $\theta_0 = 90^o$.

Our simulated *g(r)* values for the I-125 line source were found also from the accumulated result of 60 simulations. Each run of which with 5 million numbers of primaries. Values were normalized to r = 1 cm. Figure 4.2.b.1 shows the water phantom voxels and the line source for *g(r)* measurement at the center of each voxel along *y*-axis.

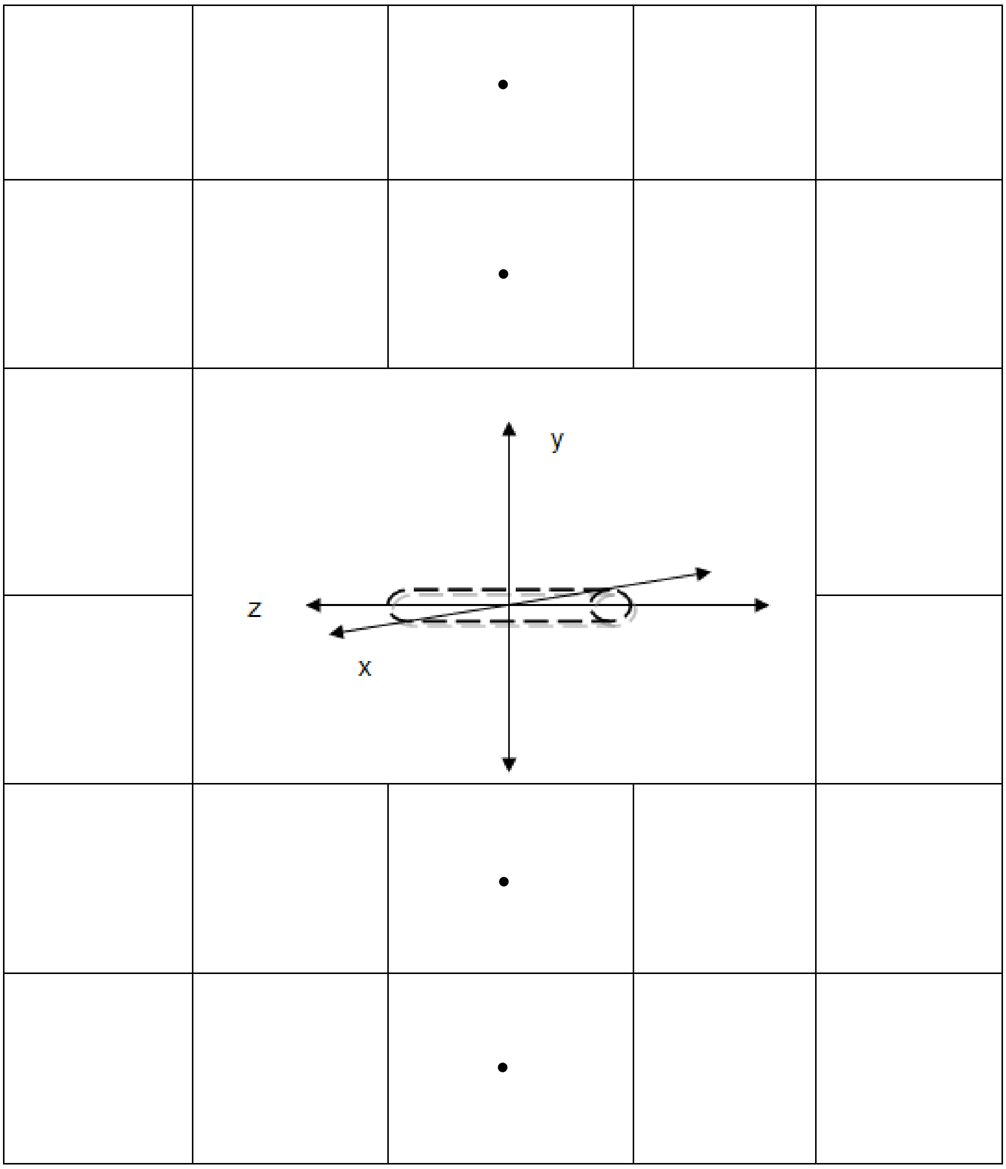


Fig 4.2.b.1: Water phantom voxels arrangement for line source *g(r)* measurement at the center of each voxel along *y*-axis.

In order to reduce statistical fluctuations, each data point was averaged over nine voxels located horizontally in the x-z plane. These nine voxels are those surrounding and including the meant voxel. Table 4.2.b.1 presents our simulated *g(r)* results of the line source along with the published *g(r)* results of the actual seed design. Our simulated *g(r)* values were drawn with the corresponding published actual seed values in order to qualitatively assess the influence of the capsule design on the *g(r)* values, compared to the pure line source. The difference in the results is clearly attributed to the fact that the simulated line source is pure without encapsulation.

Table 4.2.b.1: Comparison between simulated *g(r)* values for the line source along with published data of I-125 actual seed design.

r (cm)	Simulated GEANT4 This work	TG-43 (Rivard, et al. 2004)	EGSnrc (Taylor & Rogers, 2008)	EGSnrc (Sahoo & Selvam, 2009)
0.5	0.966	*1.030*	1.038	1.0370
1	1	1	1.002	1.0000
1.5	0.844	0.937	0.935	0.9330
2	0.729	0.857	0.856	0.8570
3	0.565	0.689	0.693	0.6970
4	0.461	0.538	0.545	0.5400
5	0.302	0.409	0.413	0.4150
6	0.190	0.313	0.314	0.3170
7	0.199	0.232	0.238	0.2370
8	0.147	0.176	0.178	0.1760
9	0.162	0.134	0.132	0.1310
10	0.018	0.0957	0.0965	0.0960

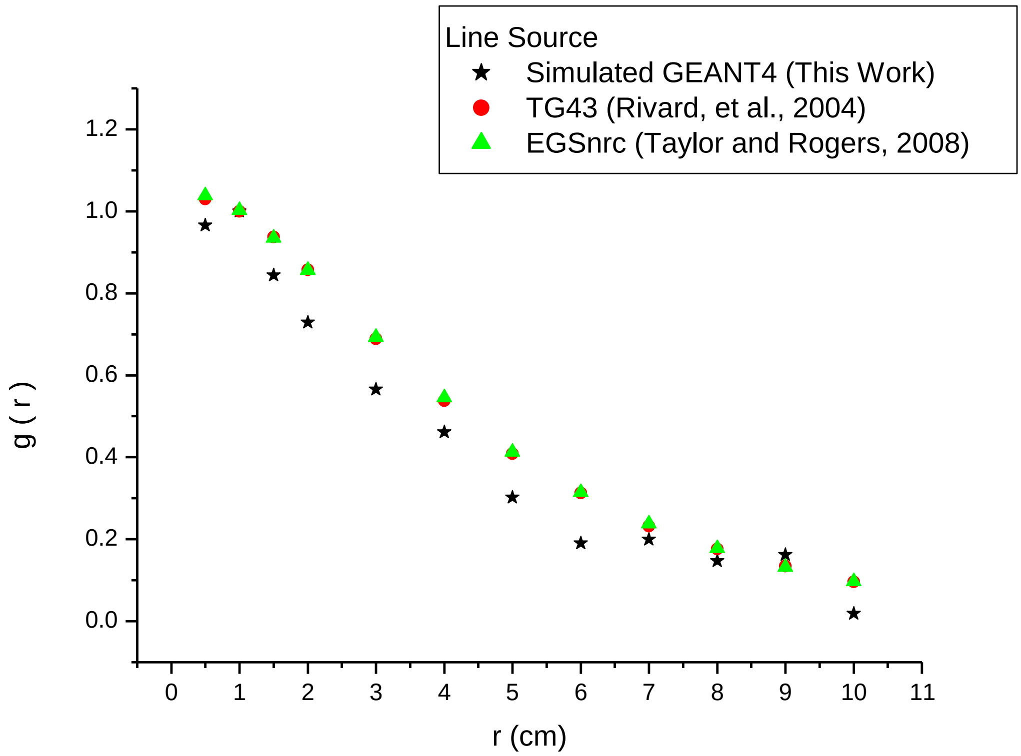


Fig 4.2.b.2. The simulated *g(r)* results of I-125 line source with corresponding published values of the actual seed design.

As mentioned above, this comparison is only needed to test the trend of the pure line source *g(r)* values compared to the trend of the actual source capsule.

The results of the simulation for the actual seed are discussed in what follows.

4.2.c Actual Seed Design

The adopted seed design was Bebig seed model I25. S06. The design of the capsule is presented Figures 4.1.d.3 and 4.1.d.4 of this chapter. It should be mentioned here, that building the capsule and the complex geometry within it was most challenging.

Both dose parameters, namely *g(r)* and $F(r,\theta)$, have been calculated from the simulation according to Eqs. 3 and 4 in Chapter Two.

4.2.c.1 The Geometry Function for the Actual Seed

In order to find the geometry function, $G_L(r,\theta)$, the *GeometricEnergy.c* code was prepared and used to calculate the relevant values at different distances from the source, and for different angles.

A comparison has been conducted between our calculated values of $G_L(r,\theta)$ and published data (Hedtjarn, et al., 2000) and (Ecker & Ziegler, BEBIGVendor, 1999). Tables 4.2.c.1.1 and 4.2.c.1.2 compare values at $\theta_0 = 90^o$ and $\theta_0 = 0^o$, respectively. Results of both tables are depicted in the Figures 4.2.c.1.1 and 4.2.c.1.2. The matching shown in the two figures, verifies the code. It should be noted here that we faced problematic values in the dosimetrical results for the actual seed design, that setback our work for few weeks. The problem turned out to be a mistake in the geometry function code. This shows the importance of verifying the codes in every step.

Table 4.2.c.1.1: Calculated vs. published geometry functions $G_L(r,\theta_0)$ at $\theta_0 = 90^o$.

r (cm)	Simulated $G_L(r,\theta_0)$	Published $G_L(r,\theta_0)$
0.1	60.094	60.1
0.2	20.538	20.5
0.3	10.059	10.1
0.5	3.848	3.85
1.0	0.990	0.99
1.5	0.442	0.44
2.0	0.249	0.249
2.5	0.160	0.16
3.0	0.111	0.111
3.5	0.082	0.082
4	0.062	0.062
4.5	0.049	0.049
5	0.040	0.04
6	0.028	0.028
7	0.020	0.020

Table 4.2.c.1.2: Calculated vs. published geometry functions $G_L(r,\theta)$ at θ = zero.

r (cm)	Simulated $G_L(r,\theta)$	Published $G_L(r,\theta)$
0.5	4.56	4.56
1.0	1.032	1.032
1.5	0.451	0.451
2.0	0.252	0.252
2.5	0.161	0.161
3.0	0.111	0.111
3.5	0.082	0.082
4.0	0.063	0.063
4.5	0.049	0.049
5.0	0.040	0.040

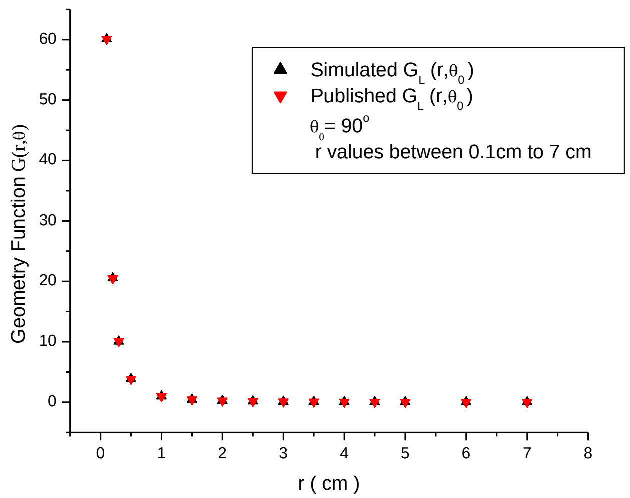


Fig 4.2.c.1.1: Comparison between calculated and published geometry function $G_L(r,\theta_0)$ at 90^0.

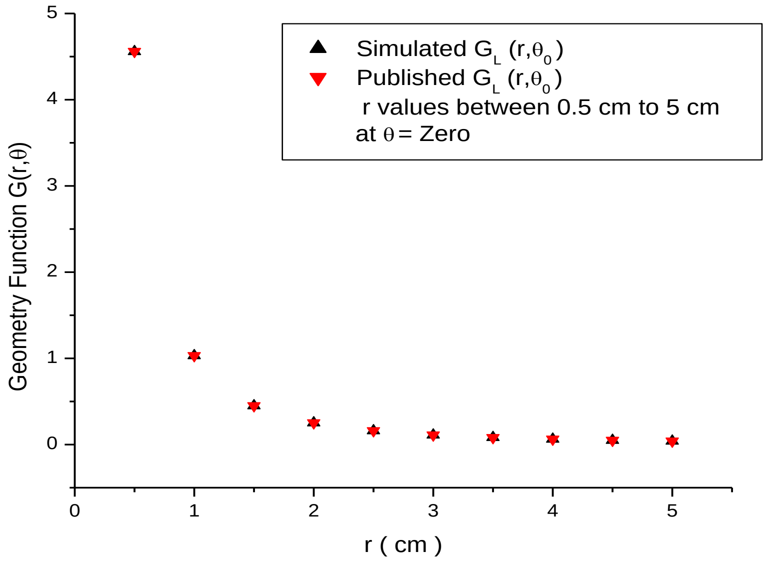


Fig 4.2.c.1.2: Comparison between calculated and published geometry function $G_L(r,\theta_0)$ at 0^0.

4.2.c.2 The Radial Dose Function *g(r)* for the Actual Seed Design

For this part, as an attempt to improve statistics, the number of simulation runs have been increased to 100, thus raising the number of primaries to 5×10^8. In addition, each *g(r)* value is again calculated as the average of nine adjacent voxels, horizontally located at the xz-plane, that include the intended voxel and its eight surroundings. However, this averaging is foreseen to affect the spatial resolution at small distances from the source, *e.g.* at r = 0.5 cm. In order to acquire more accurate results with less statistical errors, and at the same time conserving good spatial resolution needed at small distances from the source, results of the average nine voxels have been adopted for large distances where the resolution is less affected and where there is more need for improved statistics. Therefore, at close distances the values were not averaged, but rather adopted from the corresponding voxel at the intended distance.

For the 500 million primary events simulated in this work, the statistical uncertainty in energy deposition for each voxel has been calculated according to Eq. 6, where σ is the standard deviation, D_i is the dose delivered by the i^{th} primary particle to a given

voxel, and D_τ is the dose delivered by the whole *N* primary particles ($5x10^8$) to a given voxel.

$$\sigma_{D\tau} = N\sqrt{\frac{\sum_{i=1}^{N} D_i^2 - \frac{\left(\sum_{i=1}^{N} D_i\right)^2}{N}}{N(N-1)}} \quad , \qquad (6)$$

The absolute standard deviation (Eq. 6) in the simulated energy deposition in each voxel, and the corresponding percentage error have been calculated. From these values, the *g(r)* data and the associated uncertainties have been then calculated and listed in Table 4.2.c.2.1. The calculated *g(r)* values for the actual seed capsule were again fitted using a fifth order polynomial. The fitting parameters are listed in Table 4.2.c.2.2.

Table 4.2.c.2.1: The simulated *g(r)* values and the associated uncertainties.

r (cm)	*g(r)*	Standard Deviation	Percentage Error (%)
0.5	0.97207	0.00578	0.59503
1	1	0.01171	1.17068
1.5	0.94863	0.01708	1.80099
2	0.87894	0.0218	2.47971
3	0.71652	0.02958	4.12782
4	0.5163	0.03346	6.48048
5	0.41163	0.03735	9.07403
6	0.35262	0.04153	11.77735
7	0.25926	0.04251	16.39611
8	0.19608	0.03987	20.33479
9	0.11956	0.03634	30.39246
10	0.10478	0.03675	35.0766

Table 4.2.c.2.2: Fitting parameters of the actual seed design.

Fitting Parameter	Value
a_0	8.5805×10^{-1}
a_1	3.4589×10^{-1}
a_2	-2.6127×10^{-1}
a_3	5.735×10^{-2}
a_4	-5.45×10^{-3}
a_5	1.9×10^{-4}

Table 4.2.c.2.3.a and Figure 4.2.c.2.1 compare simulated to different published *g(r)* values. The statistical error bars in the figure have been calculated for the simulated data and discussed above.

On the other hand, Table 4.2.c.2.3.b and Figure 4.2.c.2.2 compare between simulated and fitted *g(r)* values, both obtained in this work. The difference between fitted and simulated data range between 0.04% to 32 % (Table 4.2.c.2.3.b). The larger difference clearly appears at larger distances from the source. The uncertainties in the simulated values, which are statistical in nature, are also plotted in Figure 4.2.c.2.2, absolutely as error bars in the top panel, and relatively as percentage errors in the bottom panel.

Table 4.2.c.2.3.a: Comparison between simulated and published TG-43 *g(r)* data for I-125 actual seed.

R (cm)	Simulated GEANT4 This work	TG43 Rivard, et al. (2004)	EGSnrc Taylor & Rogers (2008)	EGSnrc Sahoo & Selvam (2009)	MC Heintz et al. (2001)	TLD Patel et al. (2001)	MC DLC 99	MC DLC 146
							Hedtjarn et al. (2000)	
0.5	0.97207	*1.030*	1.038	1.0370	1.0289	1.094	1.03	1.03
1	1	1	1.002	1.0000	1	1	1	1
1.5	0.94863	0.937	0.935	0.9330	0.928	0.98	0.94	0.937
2	0.87894	0.857	0.856	0.8570	0.8593	0.843	0.859	0.857
3	0.71652	0.689	0.693	0.6970	0.6988	0.679	0.7	0.689
4	0.5163	0.538	0.545	0.5400	0.5481	0.524	0.548	0.538
5	0.41163	0.409	0.413	0.4150	0.4203	---------	0.42	0.409
6	0.35262	0.313	0.314	0.3170	0.3228	---------	0.323	0.313
7	0.25926	0.232	0.238	0.2370	0.2394	---------	0.239	0.232
8	0.19608	0.176	0.178	0.1760	0.1816	---------	0.182	0.176
9	0.11956	0.134	0.132	0.1310	0.133	---------	0.133	0.134
10	0.10478	0.0957	0.0965	0.0960	0.0995	---------	0.0995	0.0957

Table 4.2.c.2.3.b: Comparison between simulated and fitted *g(r)* results for I-125 actual seed.

r (cm)	Fitted Simulated GEANT4 (This work)	Simulated GEANT4 (This work)	Percentage Difference (%)
0.5	0.97251	0.97207	0.045264
1	0.99476	1	0.524
1.5	0.95644	0.94863	0.823293
2	0.88244	0.87894	0.398207
3	0.69754	0.71652	2.64891
4	0.53137	0.5163	2.918846
5	0.41297	0.41163	0.325535
6	0.33192	0.35262	5.87034
7	0.26119	0.25926	0.744426
8	0.17997	0.19608	8.21603
9	0.09651	0.11956	19.279
10	0.07095	0.10478	32.2867

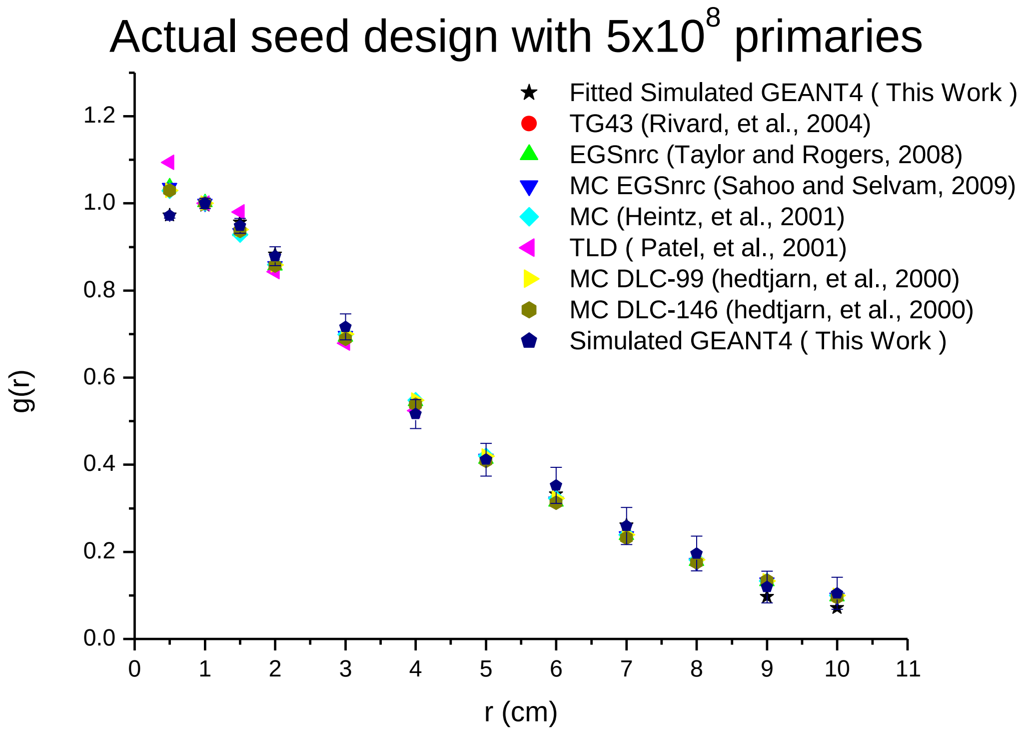


Fig 4.2.c.2.1: The simulated and published values of *g(r)* for the actual I-125 Bebig model I25.S06 seed. The error bars represent statistical fluctuations and have been calculated for the simulated data (see text).

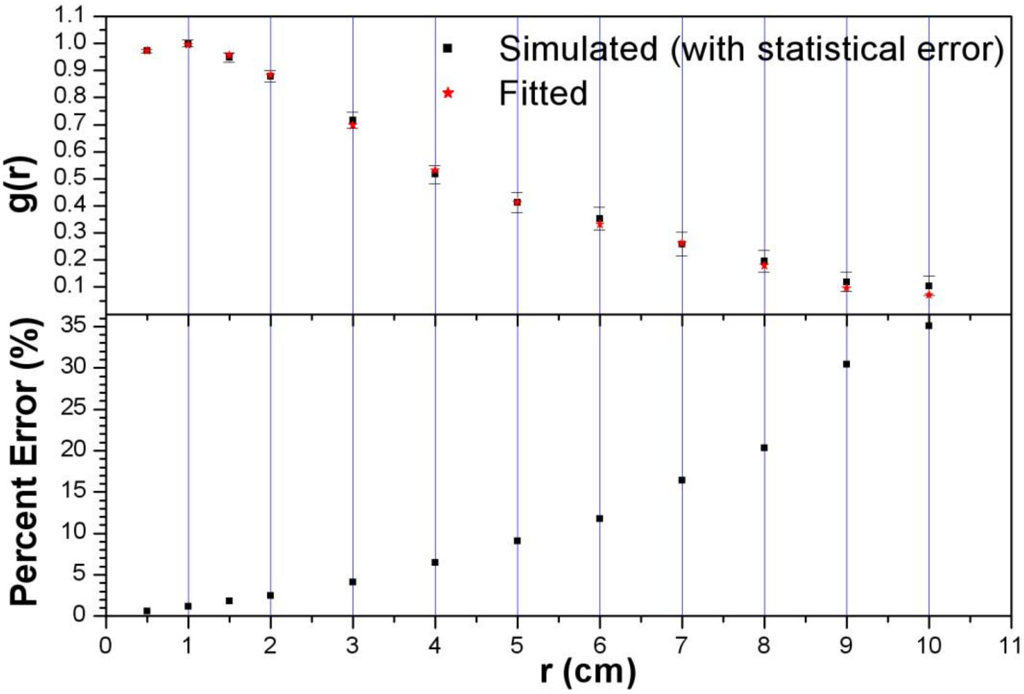


Fig 4.2.c.2.2: Comparison between simulated and fitted *g(r)* values of the actual seed design. The error bars in the top panel represent statistical uncertainties. The percentage errors are plotted in the lower panel as well.

For a more comprehensive analysis, and as our simulated results have been compared to six sets of published data (Fig. 4.2.c.2.1), these published findings seem to qualitatively agree with our results. However, there are discrepancies that can be explained in the following:

1. The EGSnrc data (Taylor and Roger, 2008) uses the incomprehensive and unrealistic approximation of not transporting the electrons, as mentioned above. This explains the deviation near and far away from the source.
2. TG-43 data is a collection of older studies subject to approximations and assumptions (Rivard, et al., 2004).
3. For the published results of the thermoluminescent dosimetry (TLD) with size of 1 mm^3 (Patel, et al., 2001), the dose was only measured up to 4.0 cm. TLD measurements show higher values than all other studies, including this work, especially at small distance (r = 0.5 cm), where *g(r)* = 1.094 and 0.97 for TLD

measurement and our work, respectively. This could be due to the energy dependence and sensitivity of the TLD.

4. The published data by Heintz, et al. (2001) also used TLD. Their results were following ours except at r = 0.5 cm. This can be attributed to the fact that their TLD measurement was performed with less resolution than ours.
5. The data by Hedtjarn, et al. (2000) follow ours as a general trend. However, they have excluded the characteristic x-rays emitted from titanium in their work.
6. Data by Sahoo and Selvam (2009) is in agreement with our work. They have used EGSnrc, while our work is based on GEANT4. A point to mention here is that they used a cut-off energy of 5 keV in their work.

4.2.c.3 The Anisotropy Function $F(r,\theta)$ of the Actual Seed Design

Results of the anisotropy function $F(r,\theta)$ are presented, in this section, for the actual I-125 source seed Bebig (I25.S06) model. It is worth mentioning here that, unlike the $g(r)$ calculations performed using averaging over nine voxels at the same y-value, the $F(r,\theta)$ results have been calculated using only one single voxel at the location specified by r and θ. Though this is on the expense of better statistics, but the procedure preserves spatial resolution. No adjacent voxel can share the same two polar coordinates.

The arrangement of water phantom voxels used to find $F(r,\theta)$ is shown in Figure 4.2.c.3.1.

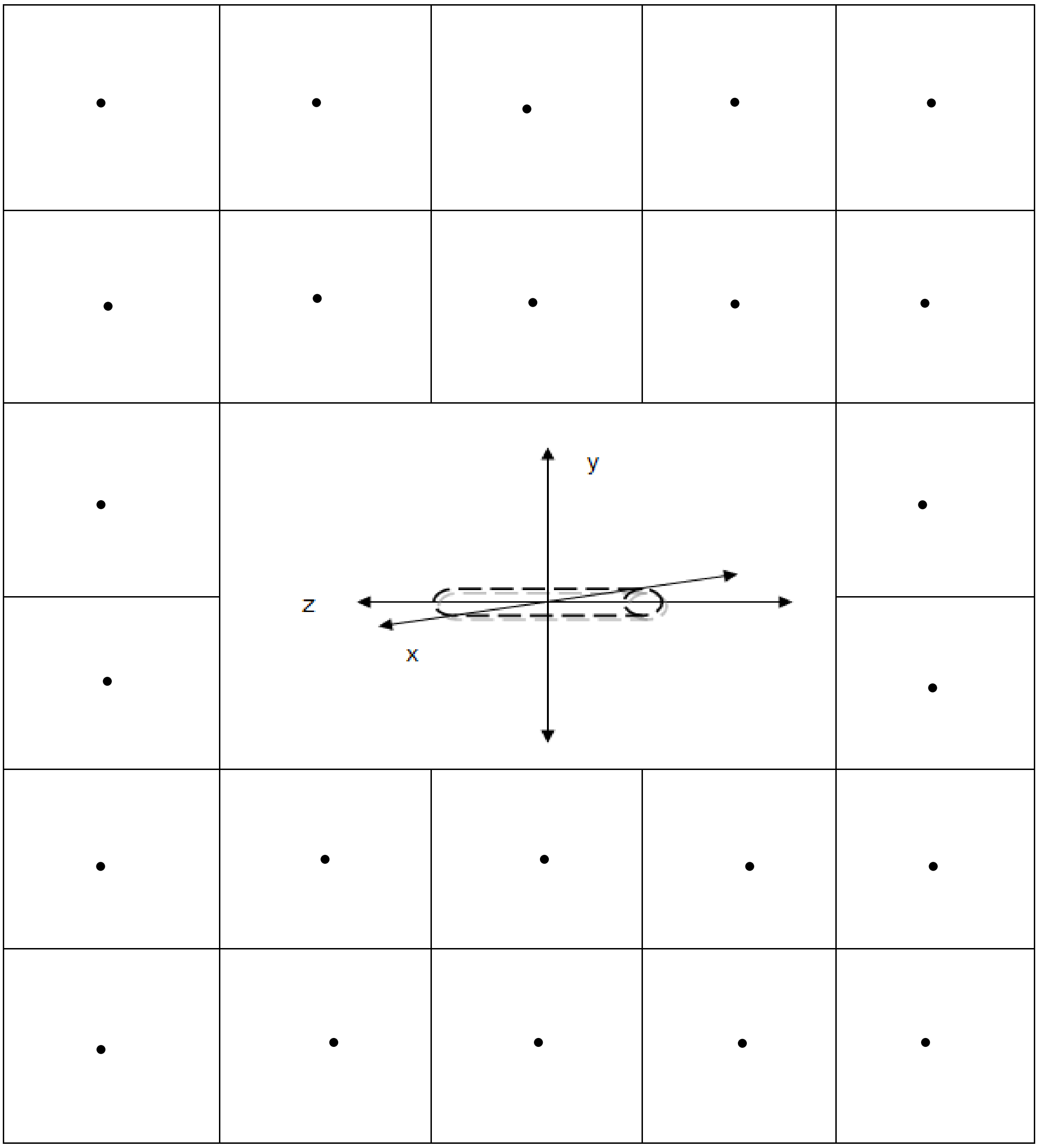


Fig 4.2.c.3.1 Water phantom voxels arrangement used the actual seed $F(r,\theta)$ measurement at the center of each voxel in the *yz*-plane.

According to Eq.4 in Chapter Two, $F(r,\theta)$ is the relative dose rate with the geometry function factored out. At every r and θ point, the dose rate is normalized to the dose rate at the same r but at $\theta = 90°$.

The simulation consisted of 86 runs totaling 430×10^6 primaries. The data is drawn in Figure 4.2.c.3.2. The simulated $F(r,\theta)$ values are plotted in the upper panel. The error bars are statistical fluctuations in the data. The corresponding percentage error is plotted in the lower panel. Clearly, this uncertainty increases as r increases due to dose fall-off.

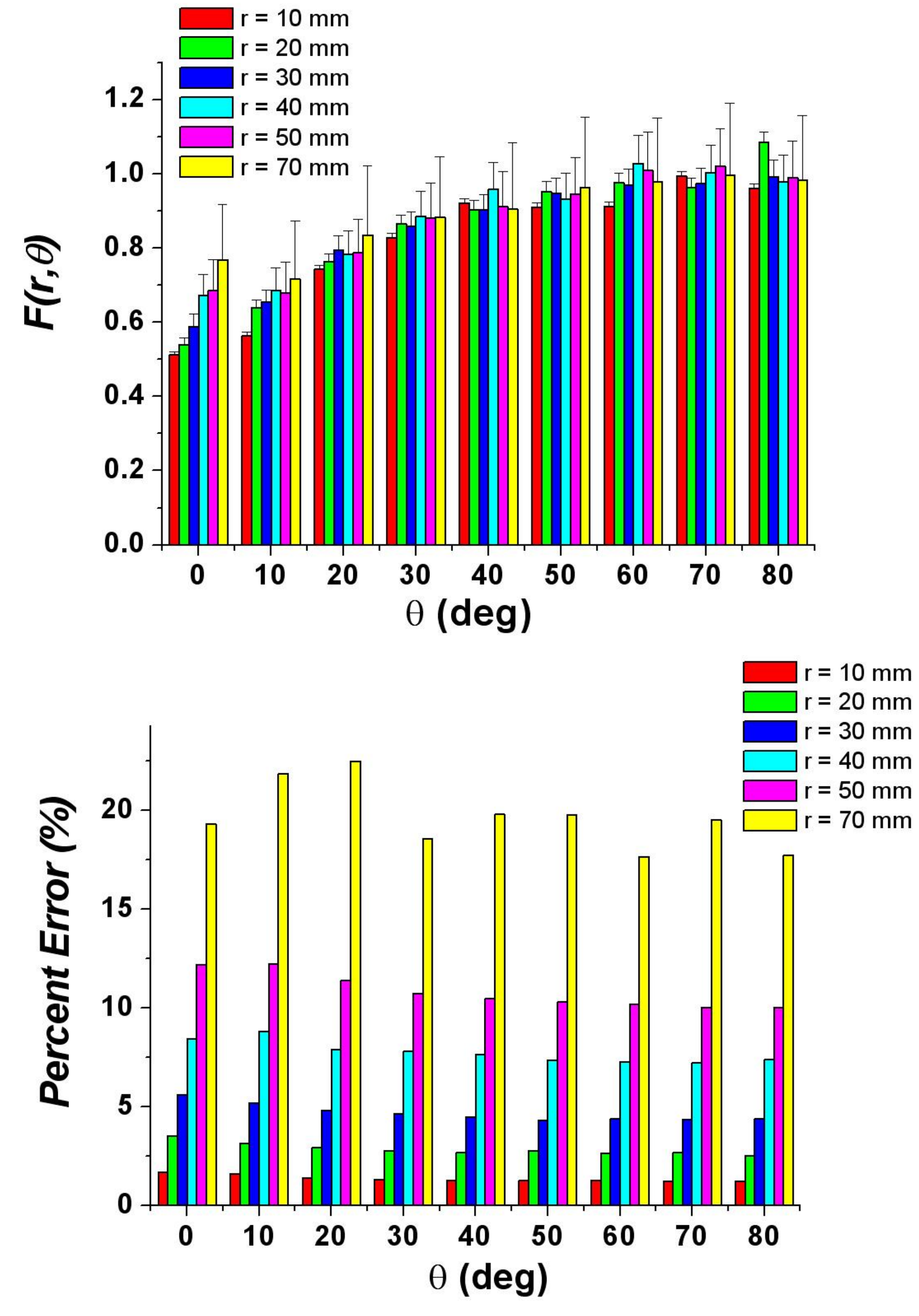


Fig 4.2.c.3.2: The simulated $F(r, \theta)$ values are plotted in the upper panel. The error bars are statistical fluctuations in the data. The corresponding percentage error is plotted in the lower panel.

Figure 4.2.c.3.3 represents the same *F(r,θ)* simulated data interpolated to form a contour 3-D plot. The edge effect of the Ti welding cap clearly causes the function to take minimum values on the *z*-axis, *i.e.* for θ = 0. It is worth noticing that at θ = 0, the function takes minimum values due to the Ti welding edge effect.

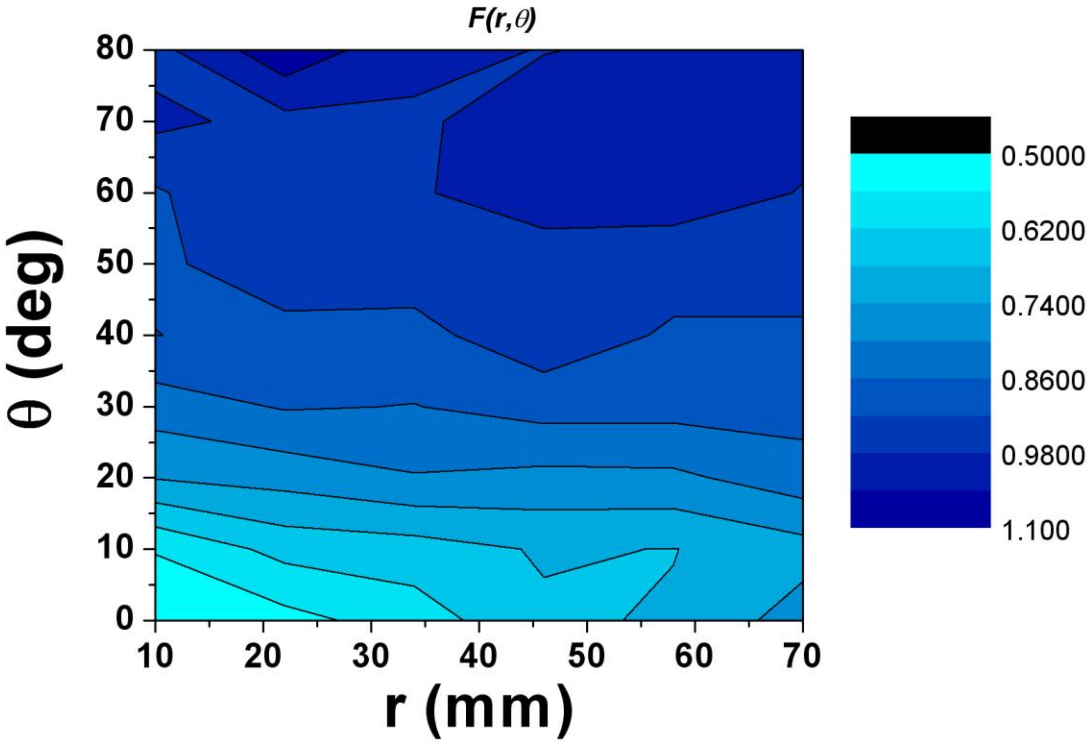


Fig 4.2.c.3.3: The *F(r,θ)* simulated data of Fig 4.2.c.3.2 interpolated to form a contour 3-D plot.

All of the simulated *F(r,θ)* data of this work have been compared to data published by Rivard, et al. (2004), Taylor and Rogers (2008) and Patel, et al. (2001). One such comparison is depicted in Fig. 4.2.c.3.4. It is worth mentioning here that:

1. Published results are in general in fair agreement with those obtained in this work, taking into consideration that the standard deviation in the simulated results increases with distance from the source. This is due to poorer statistics as the dose falls off.

2. The published TLD data (Patel, et al., 2001) were higher than all other values, including the results of this work.

3. Discrepancies observed between various published MC data themselves, as well as those of this work, could be attributed to the use of different tracking methods, cut-off energies, voxel size and definition of the main material inside the capsule, namely the ceramic. The physics implemented in this work is comprehensive compared to previous MC results, and tracking was complete in terms of including all secondary particles, namely electrons.

4. At θ = 0, the attenuation through the encapsulation, particularly through the Ti ending, played major role in decreasing the relative dose rate at close distances.

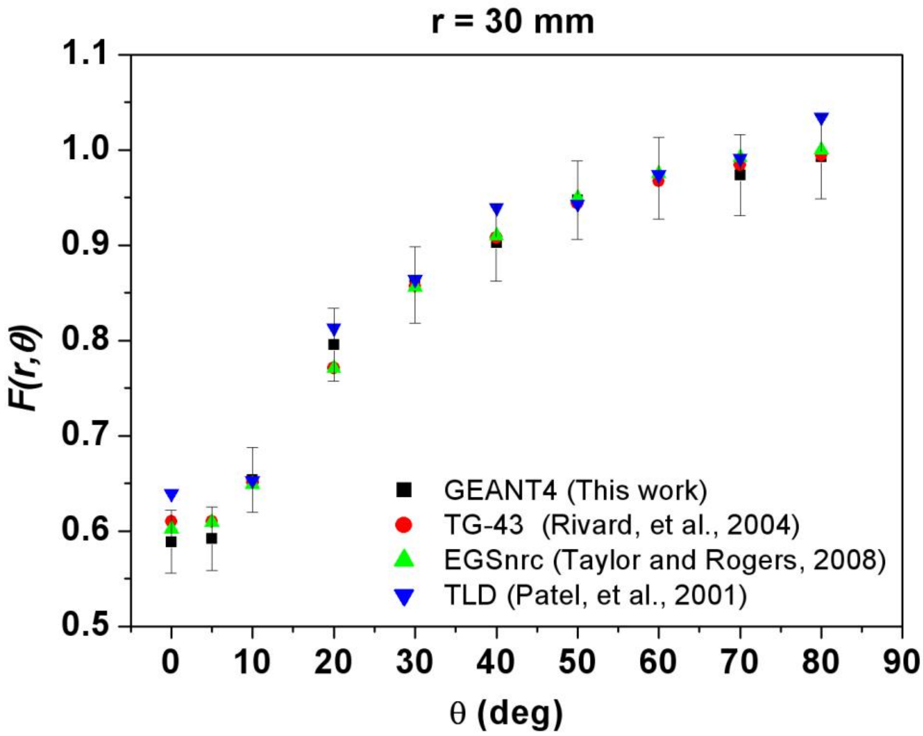


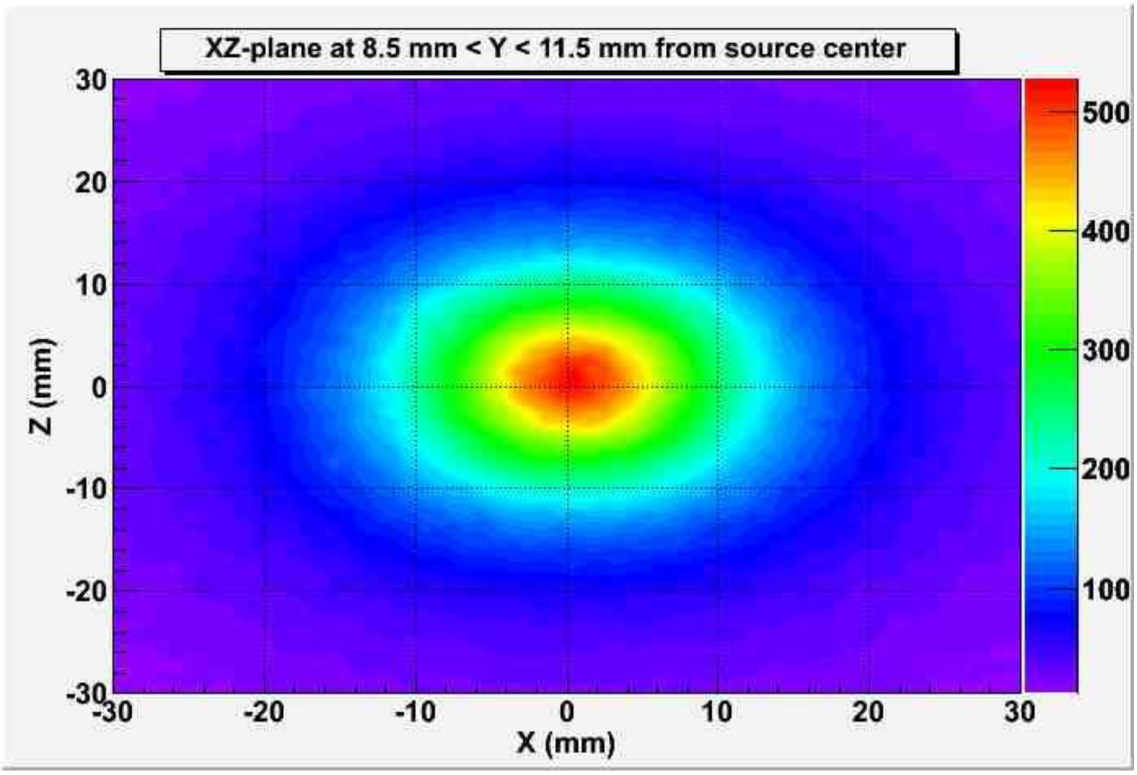
Fig 4.2.c.3.4: The simulated $F(r,\theta)$ at r = 3 cm compared to the literature.

4.3: Isodose contours

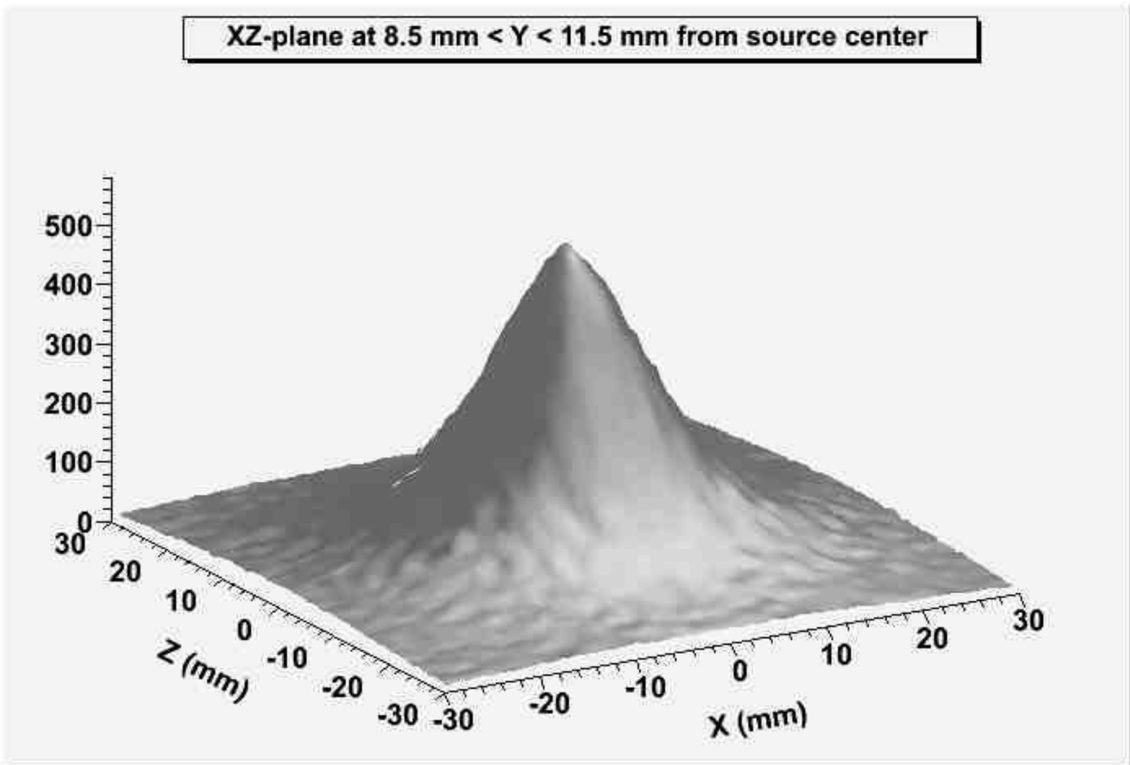
Since all of the results described so far have been extracted and calculated from deposited energy data in the phantom voxels, it is worth finalizing this work by reporting different isodose contours. These plots are either in planes parallel, or perpendicular, to the source which is positioned along the *z*-axis with its center at (0.5 mm, 0.5 mm, 0.5 mm).

Figs. 4.3.1 (a and b) depict the isodose plot acquired in a layer, three mm in thickness, placed in the *xz*-plane around *y* = 1 cm. The center of the contours is clearly shifted from the origin of coordinates since the source itself is shifted as mentioned above. On the other hand, if we consider a similar layer but in the *xy*-plane, *i.e.* located around *z* = 1 cm, we should expect to see the edge effect caused by the Ti welding cap that forms an absorber. This effect is obvious at the center of Fig. 4.3.2a and on top of the volcano-shaped 3D plot of Fig. 4.3.2b.

A final look at the isodose contours have been conducted by generating those contours on planes intersecting the source rather than being registering dose completely away from the source. Fig. 4.3.3 depicts the isodose plot on the *xz*-plane intersecting the source. The source elongation in the z-direction is clear. The edge effect caused by the Ti cap can also be identified. The sharp drop in the dose outside the source is also clearly evident. A similar run has been conducted in the corresponding *xy*-plane (Fig. 4.3.4). The symmetry along both axes inferred by the source geometry is evident. The symmetry along both directions is implied by the geometry of the source, which is modeled to be elongated in the *z*-direction.

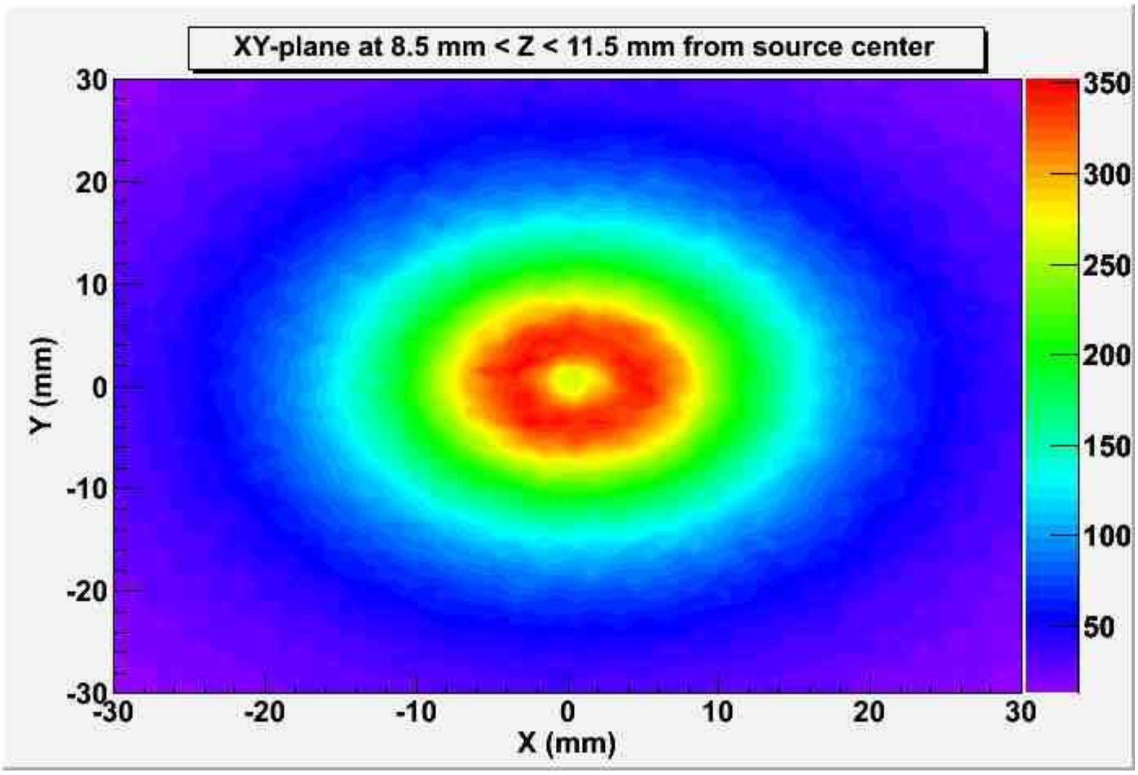


(a)

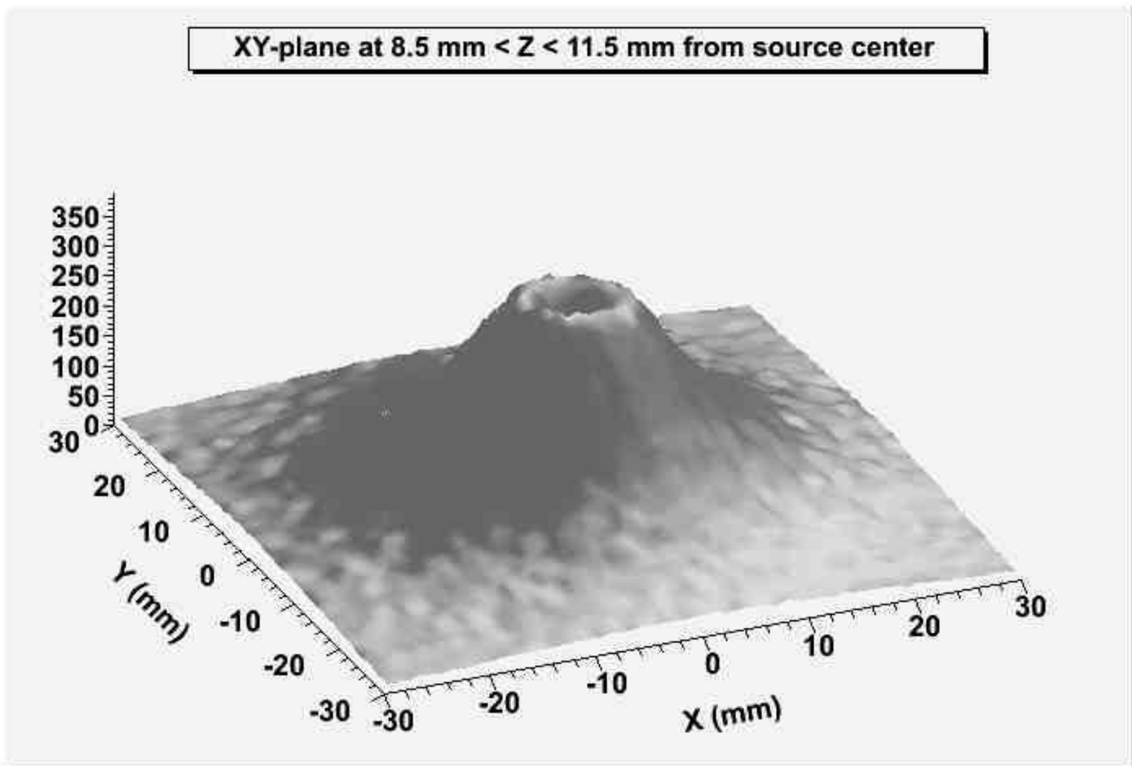


(b)

Fig 4.3.1(a and b): Isodose plot acquired in a layer, three mm in thickness, placed in the *xz*-plane around y = 1 cm.



(a)



(b)

Fig 4.3.2(a and b): Isodose plot acquired in a layer, three mm in thickness, placed in the *xy*-plane around $z = 1$ cm. The edge effect caused by the Ti welding cap that forms an absorber is obvious and manifested as a sharp drop in dose at the center.

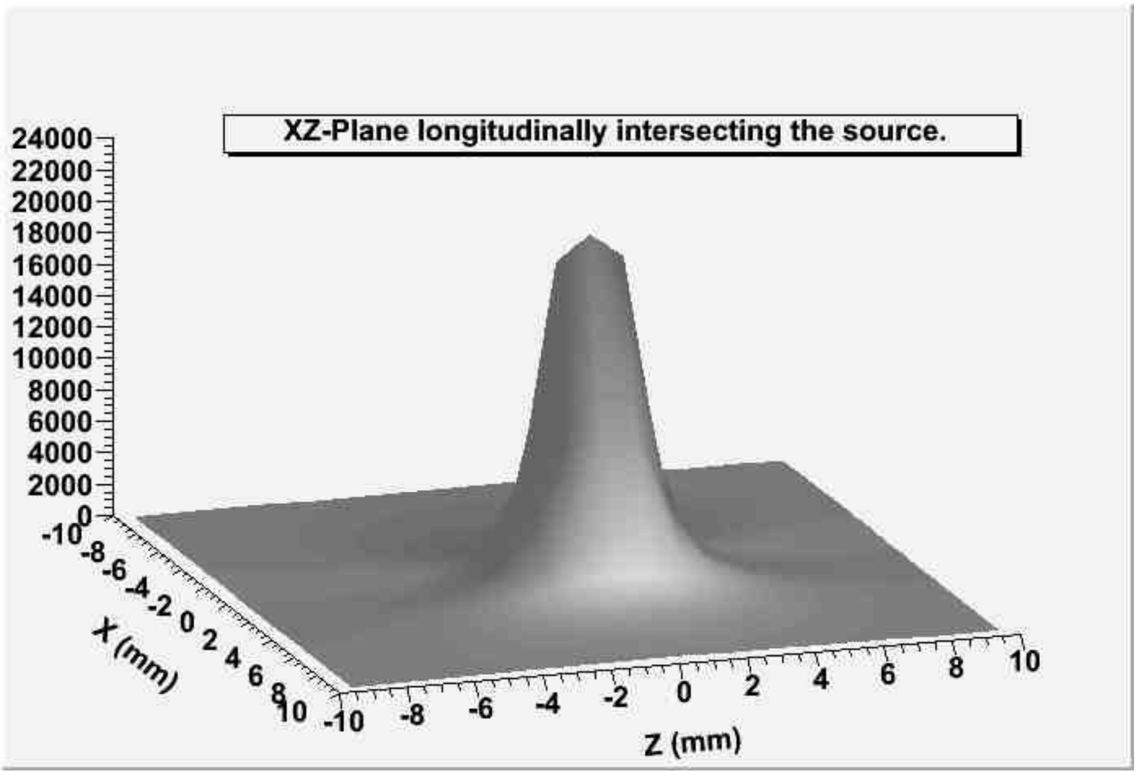


Fig 4.3.3: Dose in the *xz*-plane intersecting the source. The edge effect discussed earlier is evident along the *z*-axis.

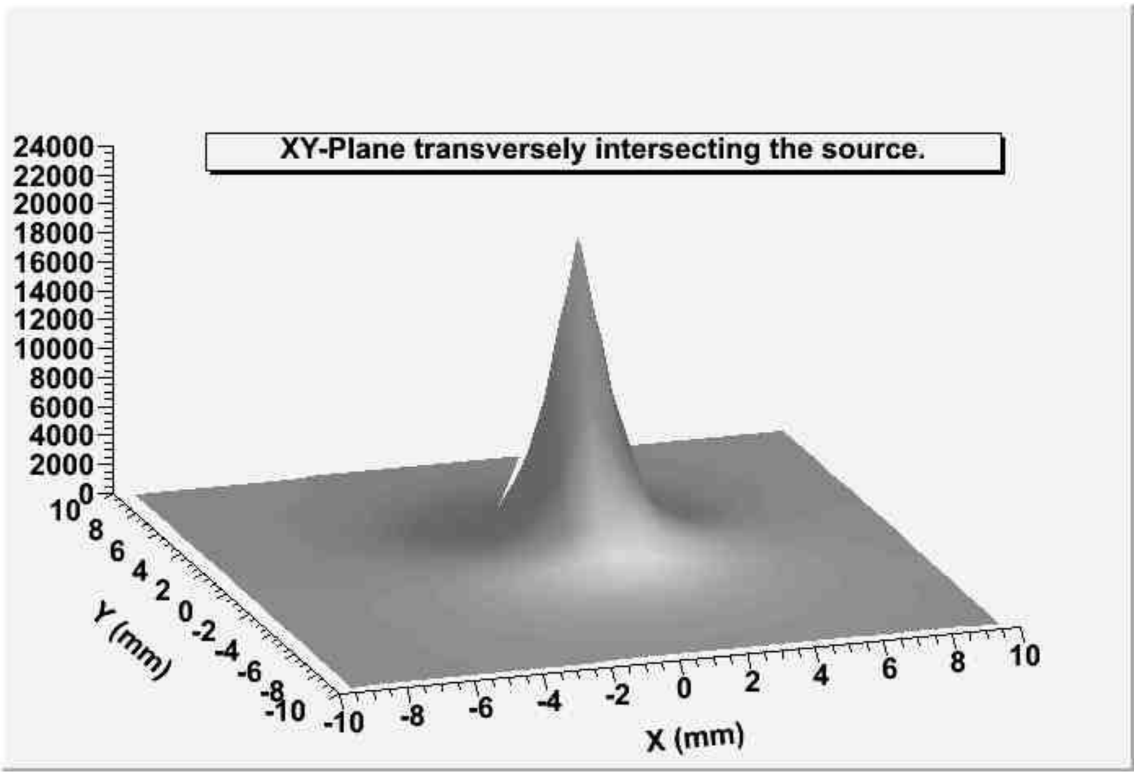


Fig 4.3.4: Dose in the *xy*-plane intersecting the source. The sharp drop in dose along both axes is evident.

CHAPTER FIVE

Summary and Conclusions

5.1 Summary

We have developed our own modeling and simulation codes which are based on GEANT4 Monte Carlo toolkit in order to calculate the dosimetric parameters for model I25.S06 I-125 source. The following forms a summary of the work:

1. The measurement phantom was a cube of 30×30×30 cm^3 of water, divided into 1 mm^3 voxels. Water is the material of choice in radiation therapy calculation as it mimics the human body.
2. The small voxel size is required to obtain high resolution. However, this high resolution requires a large number of primaries to reduce the statistical fluctuation. As such, one hundred simulation runs, five million primaries per run, and totaling $5x10^8$ primaries require a considerable computer run-time.
3. No restrictions or limitations were applied in terms of tracking the photons and the generated secondary electrons. The code kept track of all energy deposited in each voxel. In addition, comprehensive physics processes have been implemented.
4. Absorbed dose is defined as, Dose (Gy) = Deposited Energy (J) / Mass (kg). Since the mass of each voxel was the same (all voxels have the same volume and density), then the dose is directly proportional to energy deposition.
5. Before data has been acquired, the codes developed in this work were verified (benchmarked) in every step.
6. We proceeded from point source to pure I-125 line source, ultimately to the final actual model under investigation.

7. For the radial function *g(r)*, each data point at distance *r* from source was represented by the average value of nine voxels (in *xz*-plane) around and including it. This was used to decrease statistical fluctuation without compromising accuracy since all voxels are located at the same $y = r$ value.
8. The above averaging technique was not used for the anisotropy function $F(r,\theta)$, because it would have masked the true value at each data point. Instead, larger number of primaries and longer run times have been used.
9. Isodose contours have been generated which verify the expected behavior at different layers and directions from the source.

5.2 Conclusions

In certain cases the data of this work exhibit agreement with previously published data, whereas in other cases discrepancies have been found.

1. Point source:
    a. For a point source of I-125, our work showed a 7% higher value for *g(r)* at 5 mm from the source compared to a previously published data acquired using different MC codes (Taylor and Rogers, 2008). At $r > 4$ cm, the trend was reversed, and our data was less than the published values. This can be explained by the fact that the previously published data suppressed the electron transport within the water, and thus artificially affect their results. In this work, complete, comprehensive and time consuming tracking of all secondaries has been applied.
    b. A fifth order polynomial fit is proposed for *g(r)*, with the following fitting parameters: $a_0 = 1.096$, $a_1 = -2.428\times10^{-2}$, $a_2 = -6.623\times10^{-2}$, $a_3 = +9.67\times10^{-3}$, $a_4 = -3.178\times 10^{-4}$ and $a_5 = -6.676\times 10^{-6}$.

2. Actual seed: For distances r $\geq$ 1 cm, our results for the actual seed design are in excellent agreement with seven recently published data. All studies disagreed at the closer distance of 5 mm. Six studies reported values in the range of 1.029 – 1.038, with a median value of 1.03. One study, which is based on TLD, showed the highest value of *g(r)* of 1.094, representing 6% higher than the median value of the above six studies. In contrast, our work reports the lowest value of *g(r)* at 5 mm of 0.973; 5.5% lower than the median value of the six other studies.

   Near the source, dosimetry is affected greatly by the method of measurement and the design of the source. TLD crystals, being non water equivalent, could have over responded with the flux of photons and electrons coming out from the capsule at this close distance, hence the seemingly larger dose.

   The other studies, including our work, are Monte Carlo based with the detector being the water phantom itself. However, variations occur within each study on what approximations to be used in order to decrease the run time. This parameter affects the results of each study. This was discussed in details in Chapter 4. In addition, a major component of I25.S06 capsule is ceramic, in which I-125 is embedded. There are various descriptions (effective Z, component and weight of each element, and density) of ceramic, and those variations bear a huge impact on the calculated dose at 5 mm.

3. The anisotropy function $F(r,\theta)$ results have been found for the actual seed design Bebig model I25.S06. Obtaining this data was tedious as up to 500 million primaries were used to decrease statistical fluctuations.

   a. Plotting $F(r,\theta)$ at a constant r and variable θ. This was used to compare our work with previously published data.

b. Comparison showed fair agreement between the results of this work and previous works. However, at some points, discrepancies were noticed without an observable trend. Both our work and the TLD-based study seemed to deviate from the bulk of the published data, at certain, seemingly, random points. On the other hand, some MC based studies didn't publish the data at certain distances, and there was no mention of statistical accuracy in these studies.

c. The 3D plot of $F(r,\theta)$ shows that at the edges of the source, i.e. $\theta = 0$ degrees, the values are at their lowest. This is due to the attenuation of photons through the titanium edges of this capsule design. The same feature has been also verified using the isodose contours plot in the *xy*-plane.

4. For the actual seed design, comprehensive assessment of the standard deviation has been performed.

In summary, our research objectives regarding the calculations of the dosimetric parameters, namely $g(r)$ and $F(r,\theta)$, for a clinical type of I-125 capsule were achieved. We have demonstrated that in certain cases, our approach of comprehensive MC simulation could yield more accurate results compared to other available published data, whereas in other cases, our results were in good agreement with the literature.

5.3 Future Work

After GEANT4 has been benchmarked to work with I-125 clinical seeds, future work can concentrate on particular applications of those seeds. The use of the seeds in the treatment of eye tumors and the treatment of prostate cancer are examples. Each treatment has its own uniqueness, and as in almost all clinical situations, in vivo measurement inside the patient is impossible. Classical calculation of dose is based on equations that use many assumptions. As such, Monte Carlo simulation becomes a powerful alternative to substitute in vivo dosimetry, and to provide case by case verification of dose. This is conditioned of course by the accurate coding of the geometry under study.

We propose that the application to be considered next is the treatment of eye cancers, known as plaque brachytherapy. The simulation phantom could be the eye model. Different objectives could be achieved, such as investigating the effect of the gold plaque and silastic–plastic seed carriers on the photons emitted from each seed, calculating the dose deposited by the tumor, calculating the dose delivered at all the critical structures in the eye such as sclera, retina, optical disk, and lens.

For that to be achieved, Monte Carlo simulation should be designed according to the following aspects:

1. A code should be developed to reconstruct the anatomy of the eye and the identification of the various structures within it.
2. Another code is needed to reconstruct the gold plaque, silastic-plastic carrier and the seed design.
3. Placement of I-125 seeds within the plaque.
4. Placement of the gold plaque on the eye.

5. MC calculation of the dose rate to the tumor from which the total time of implant should be calculated.

6. The dose delivered to the critical structures within the eye should be found.

7. Comparison of the results obtained through MC, with the results obtained through the Collaborative Ocular Melanoma Studies (COMS) recommended approximations, should be done.

Eventually, a Monte Carlo based planning system for plaque therapy could be developed.

REFERENCES

An Ecker & Ziegler Company**, BEBIG**, (1999), IsoSeed **I-125(I25.S06) Instructions for Use**, The vendor, Berlin, BEBIG Rev. 05/2002 EU-EN.

Astrahan, M. Luxton, G. Jozef, G . Kampp, T. Liggett, P. Petrovich, Z. and apozink, M. (1989), **An interactive treatment planning system for ophthalmic plaque radiotherapy**. Intl. J. Radiat. Oncol. Biol. Phys, 18 (3), 679-687.

Astrahan, M. Luxton , G. Jozef, G. Liggett, P. and Petrovich , Z. (1990), Optimization of ^{125}I ophthalmic plaque brachytherapy. **Med. Phys** 17 (6), 1053-1057.

Berger, M. Hubbell, J. Seltzer, S. Chang, J. Coursey, J. Sukumar, R. and Zucker, D. NIST XCOM: Photon Cross Sections Database, **http://physics.nist.gov/PhysRefData/Xcom/Text/XCOM.html.**

Berger, Marsha (1968), Energy Deposition in Water by Photons from Point Isotropic Sources, **J. Nucl. Med**.2 **(9)**, 15-25.

Burns, G. and Raeside, D. (1983), Monte Carlo estimates of specific absorbed fractions for an 1-125 point source in water**, Med. Phys**. 10 (2),197-198.

Calatayud, J. CabaÑero, D. and Pallarés F, (2009), Monte Carlo Application in Brachytherapy Dosimetry, Radiotherapy and Brachytherapy, NATO Science for Peace and Security Series B: Physics and Biophysics, **Springer Netherlands** ,Volume . ISBN 978-90-481-3095-5, 239-250.

Chu *S*, Ekström *L*, and Firestone *R* ,(1999),The Lund/LBNL Nuclear Data Version 2.0, from **http://nucleardata.nuclear.lu.se/nucleardata/toi/.**

Dyk J, Barnett R, Cygler J, and Shragge P, (1993), Commissioning and Quality Assurance of treatment planning computers, **Int. J. Radiation Oncology Biol. Phys**. 26 (2), 261-273.

Frank, S. Pisters, L. Davis, J. Lee, A. Bassett, R. and Kuban, D. (2007), An Assessment of Quality of Life Following Radical Prostatectomy, High Dose External Beam Radiation Therapy and Brachytherapy Iodine Implantation as Monotherapies for Localized Prostate Cancer, **The Journal of Urology,** 177(6), 2151-2156.

Hedtjarn H, Carlsson G, and Williamson J, (1999), Monte Carlo-Aided Dosimetry of the Symmetra Model I25.S06 125I, Interstitial Brachytherapy Seed, **Med. Phys.** 27(5),1076-1085.

Heintz, B. Wallace, R. and Hevezi, J. (2001), Comparison of I-125 Source Used for Permanent Interstitial Implants, **Med. Phys**. 28(4), 671-682.

Hidajat N, Stupavsky A, Gellermann J, Kreuschne M, Stahl H, Wust P, Felix R, and Schroeder R, (2005), Intraluminal Brachytherapy of DeNovo TIPS: A Prospective Randomized Double-Blind Study, from **http://www.ajronline.org/cgi/content/full/186/4/1133.**

Khan, Faiz (2003), **The Physics of Radiation Therapy**, Third Edition. Baltimore: Williams-Wilkins.

Knutsen, S. Hafslund, R. Monge, O. ValEn, H. Muren, L. Rekstad, B. Krohn, J. and Dahil, O. (2001), Dosimetric Verification of A Dedicated 3D Treatment Planning System for Episcleral Plaque Therapy, **Int. J. Radiation Oncology Biol. Phys**. 51(4), 1159–1166.

Kubo, Hideo (1983), Comparison of Two Independent Exposure Measurement Techniques for Clinical I-125 Seeds. **Med. Phys**, (2), 221-224.

Kubo, Hideo (1984), Exposure Contribution From T\Kx Rays Produced in the Titanium Capsule of the Clinical 1-125 Seed, **Med. Phys**. 12 (2), 215-220.

Meigooni, A.Hayes, J., Zhang, H. and Sowards, K. (2002), Experimental and Theoretical Determination of Dosimetric Characteristics of IsoAid ADVANTAGE™ ^{125}I Brachytherapy Source, **Med. Phys**. 29(9), 2152-2158.

Nath, R. Anderson, L. Luxton, G. Weaver, K. Williamson, J. and Meigooni, A. (1995), Dosimetry of interstitial brachytherapy sources: Recommendations of the AAPM Radiation Therapy Committee Task Group No. 43, **Medical Physics**. 22 (2), 209-233.

Radiology associates of Hollywood**,** INTRAVASCULAR BRACHYTHERAPY, from **http://rahradiationoncology.com/serv- ivb.htm.**

PERL, JOSEPH (2007), NORTH AMERICAN MEDICAL PHYSICS APPLICATIONS OF THE GEANT4 SIMULATION TOOLKIT , Astroparticle, Particle, Space Physics, Detectors and Medical Physics Applications 10th conference, Italy, 19/Nov/2007, from **http://villaolmo.mib.infn.it/ICATPP10th_2007/Software%20Applications/Perl.pdf**

Ravinder, Nath (2005), Sources and Delivery Systems I: Radionuclides, **American Association for Medical Physics Summer School.** Yale University.

Ray, S. Bhatnagar, R. Hartsel, L. and Desai, G. (1998), Review of Eye Plaque Dosimetry Based on AAPM Task Group 43 Recommendations. American Association of Physicists in Medicine, **Int. J. Radiation Oncology Biol. Phys,** 41(3), 701-706.

Rivard, M. Coursey, B. DeWerd, L.Hanson, W. Saiful Huq, M. Ibbott, G. Mitch, M. Nath, R. and Williamson, J. (2004), Update of the AAPM Task Group No. 43 Report: A Revised AAPM Protocol for Brachytherapy Dose Calculations, **Med. Phys**. 31(3), 633-674.

Sahoo, S. and Selvam, T. (2009), An EGSnrc Investigation of The Air- Kerma Strength, Dose Rate Constant, and Radial Dose Function of I-125 Brachytherapy Sources. **Radiol Phys Technol**, (2), 198–204.

Shleien, B. Salback, L. and Birky, B. (1998), **Hand Book of Health Physics and Radiological Health**, (3rd ed).United States of America: Williams & Wilkins.

Siwek, R. O'Brien, P. and Leung, P. (1991), Shielding effects of Selectron Applicator and Pellets on Isodose Distributions, **Radiotherapy and Oncology**, Elsevier , 20(2), 132-138.

Solberg, T. Demarco, J. and Hugo, G. (2002), Dosimetric Parameters of Three New Solid Core I-125 Brachytherapy Sources. **JOURNAL OF APPLIED CLINICAL MEDICAL PHYSICS**, (3), 119-134.

Soulié, J. (2007), C++ Language Tutorial, from **http://www.cplusplus.com/doc/tutorial/.**

Sowards, Keith (2007), Monte Carlo Dosimetric Characterization of The IsoAid Advantage Pd^{103} Brachytherapy Sources. **JOURNAL OF APPLIED CLINICAL MEDICAL PHYSICS**, (8), 18-25.

Sowards, K. and Meigooni, A. (2002), A Monte Carlo Evaluation of the Dosimetric Characteristics of the Best Model 2301 I^{125} Brachytherapy Source. **Applied Radiation and Isotopes**, (57), 327–333.

Suntharalingam, N. Podgorsak ,E. and Tolli, H . (2006), Brachytherapy Physical and Clinical Aspects, Chapter 13, Vienna: International Atomic Energy Agencyof the IAEA publication, (ISBN 92-0-107304-6).from **http://www-naweb.iaea.org/nahu/dmrp/pdf_files/slides/Ch_13_MacForm.pdf.**

Taylor, R. and Rogers, D. (2008), More Accurate Fitting of ^{125}l and ^{103}Pd Radial Dose Functions, **Medical Physics**.35 (9), 4242-4250.

The National Nuclear Data Center NNDC, (2011), Nuclear Physics Data for Basic Nuclear Research and for Applied Nuclear Technologies, from **http://www.nndc.bnl.gov/**

The Free Encyclopedia, Wikipedia, from **http://en.wikipedia.org/wiki/Geant4**

Geant4 User's Guide for Application Developers, (2007), from **http://geant4.cern.ch/G4UsersDocuments/UsersGuides.**

Prostate Brachytherapy Advisory Group website (2007), Prostate Brachytherapy, from **(http://www.prostatebrachytherapyinfo.net/PAT21.html).**

Root team, Users Guide 5.21, (2008) from, **rootdoc@root.cern.ch.**

UCLA Department of radiation oncology, Brachytherapy **(**HDR) / Head and Neck Cancer, Los Angeles, **http://radonc.ucla.edu/body.cfm.**

University College London, Target Trial-Targeted Interoperative Radiotherapy for Breast Cancer, from **http://www.ucl.ac.uk.**

تحديد الخصائص الإشعاعية والجرعة الممتصة للنظير I-125 المستخدم في المعالجة الإشعاعية الداخلية

إعداد
تهاني سليمان العقرباوي

المشرف
الدكتور جمال محمود شرف

المشرف المشارك
الدكتور سائد عودة دبابنة

ملخص

بدأ الإستخدام الطبي لنظير اليود 125 المشع عام 1980، حيث تم وضع العنصر المشع داخل كبسولات، كل كبسولة منها طولها 4.5 مم والجرعة الإشعاعية تقاس من 5- 10مم من مركز الكبسولة. إن حساب الجرعات الإشعاعية التقليدي في الأغشية والأوساط المختلفة يعتمد على كثير من التقريبات التي تؤثر على دقة القياسات، هذا مع عدم أخذ توزيع العنصر المشع داخل الكبسولة بعين الإعتبار، حيث أن التوزيع للعنصر المشع غير منتظم مما يؤثر على دقة حساب الجرعات الإشعاعية حول الكبسولة. وحيث أن إستخدام الكبسولة في علاج سرطانات العين، على سبيل المثال، يحتاج إلى كثير من الدقة، فإن هدف هذه الدراسة هو حساب الجرعة الإشعاعية الناتجة من نوع معين من الكبسولات المستخدم بشكل شائع لنظير اليود 125، بدون اللجوء لأي تقريب كما جرت العادة سابقاً، ليتسنى حساب الجرعة الإشعاعية في الأغشية بشكل دقيق وتقدير المدة الزمنية اللازمة للمعالجة الداخلية بالنظير المشع بشكل أكثر دقة. بذلك فإن الأهداف الرئيسية لهذا البحث هي حساب العوامل المؤثرة بالجرعة الإشعاعية للكبسولة النشيطة إشعاعياً، بواسطة محاكاة مونتي كارلو. إن هذه العوامل هي اقتران الجرعة الإشعاعية الشعاعي، وإقتران الجرعة الإشعاعية الغير متجانس.